

Sensitivity to Triple Higgs Couplings via Di-Higgs Production in the RxSM at the (HL-)LHC and future e^+e^- Colliders

F. ARCO^{1*}, S. HEINEMEYER², M. MÜHLEITNER³,
A. PARRA ARNAY², N. RIVERO GONZÁLEZ⁴ AND A. VERDURAS SCHAEIDT¹

¹*Deutsches Elektronen-Synchrotron DESY, Notkestr. 85, 22607 Hamburg, Germany*

²*Instituto de Física Teórica (UAM/CSIC), Universidad Autónoma de Madrid,
Cantoblanco, 28049, Madrid, Spain*

³*Institute for Theoretical Physics, Karlsruhe Institute of Technology, 76128, Karlsruhe,
Germany*

⁴*Departamento de Física Teórica, Universidad Complutense de Madrid, 28040 Madrid, Spain*

Abstract

The real Higgs singlet extension of the Standard Model (SM) without Z_2 symmetry, the RxSM, is the simplest extension of the SM that features a First Order Electroweak Phase Transition (FOEWPT) in the early universe. The FOEWPT is one of the requirements needed for electroweak baryogenesis to explain the baryon asymmetry of the universe (BAU). Thus, the RxSM is a perfect example to study features related to the FOEWPT at current and future collider experiments. The RxSM has two \mathcal{CP} -even Higgs bosons, h and H , with masses $m_h < m_H$, where we assume that h corresponds to the Higgs boson discovered at the LHC. Our analysis is based on a benchmark plane that ensures the occurrence of a strong FOEWPT, where $m_H > 2m_h$ is found. In a first step we analyze the di-Higgs production at the (HL-)LHC, $gg \rightarrow hh$, with a focus on the impact of the trilinear Higgs couplings (THCs), λ_{hhh} and λ_{hhH} . The interferences of the resonant H -exchange diagram involving λ_{hhH} and the non-resonant diagrams result in a characteristic peak-dip (or dip-peak) structure in the m_{hh} distribution. We analyze how λ_{hhH} can be accessed, taking into account the experimental smearing and binning. We also demonstrate that the approximation used by ATLAS and CMS for the resonant di-Higgs searches may fail to capture the relevant effects and lead to erroneous results. In a second step we analyze the benchmark plane at a future high-energy e^+e^- collider with $\sqrt{s} = 1000$ GeV (ILC1000). We demonstrate the potential sensitivity to λ_{hhH} via an experimental determination at the ILC1000.

*emails: francisco.arco@desy.de, Sven.Heinemeyer@cern.ch, margarete.muehleitner@kit.edu,
andrea.parra@estudiante.uam.es, nestoriv@ucm.es, Alain.Verduras@desy.de

1 Introduction

The discovery of a new scalar particle with a mass of ~ 125 GeV by ATLAS and CMS [1–3] is in agreement — within the experimental and theoretical uncertainties — with the predictions for the properties of the Standard Model (SM) Higgs boson. Furthermore, no conclusive sign of Higgs bosons beyond the SM (BSM) has been observed so far. The experimental results for the couplings of the Higgs boson discovered at the LHC with a mass of about ~ 125 GeV, h_{125} , are known up to now to an experimental precision of roughly $\sim 10 - 20\%$, leave ample room for interpretations in BSM models. On the other hand, the SM fails to address various major existing observations in nature. One of the most interesting open questions concerns the origin of the matter-antimatter asymmetry of the Universe, which (according to the measured value of the mass of the Higgs boson) cannot be explained in the SM [4]. Models featuring extended Higgs sectors could allow for the generation of the baryon asymmetry of the Universe (BAU) via electroweak (EW) baryogenesis [5]. Here, a key ingredient is the realization of a First Order Electroweak Phase Transition (FOEWPT) that can take place in models with BSM Higgs sectors in the early universe when a tunneling from one minimum of the Higgs potential to a deeper one occurs [6–13]. Such a FOEWPT fulfills one of the three Sakharov conditions required for EW baryogenesis [14]. Consequently, one of the main tasks of present and future colliders will be to determine whether the observed scalar bosons part of the Higgs sector of an extended model.

In contrast to the Higgs couplings to the SM third generation fermions and to the gauge bosons, the trilinear Higgs self-coupling λ_{hhh} remains to be determined, where we will use the abbreviation $\kappa_\lambda \equiv \lambda_{hhh}/\lambda_{\text{SM}}$ in the following to quantify possible deviations from the SM value λ_{SM} . So far it has been constrained by ATLAS [15] to be inside the range $-1.2 < \kappa_\lambda < 7.2$ at the 95% C.L. and $-1.39 < \kappa_\lambda < 7.02$ at the 95% C.L. by CMS [16], both assuming a SM-like top-Yukawa coupling of the discovered Higgs boson at 125 GeV. Many BSM models can still induce significant deviations in the trilinear coupling λ_{hhh} of the 125 GeV Higgs boson with respect to the SM value, while all other experimental and theoretical constraints are fulfilled, see, e.g., Ref. [17] for a recent overview. For reviews on the measurement of the triple Higgs couplings at future colliders see for instance Refs. [18, 19]. In case a BSM Higgs sector manifests itself, it will be a prime task to measure not only λ_{hhh} , but also the other BSM triple Higgs couplings (THCs) that can be realized in the model. First studies for the (HL-)LHC in this direction can be found in Refs. [20, 21].

One of the simplest extensions of the SM Higgs sector is the Higgs-Singlet extension of the SM (RxSM) [22–25]. A real singlet, \mathcal{S} , is added to the SM Higgs sector with the doublet \mathcal{H} , leading to two physical Higgs bosons after electroweak symmetry breaking. We will assume that the lighter one, h , corresponds to the Higgs-boson observed at the LHC, whereas the heavier one, H , has escaped detection so far. The model can be realized with or without a Z_2 symmetry, under which $\mathcal{H} \rightarrow \mathcal{H}$ and $\mathcal{S} \rightarrow -\mathcal{S}$. If no Z_2 symmetry is imposed, a linear and a cubic term in \mathcal{S} is allowed. In Ref. [6] it was shown that in this case the RxSM can exhibit a FOEWPT in the early universe. Consequently, the RxSM constitutes the simplest Higgs-sector extension featuring a FOEWPT. In Refs. [7, 9, 25] it was demonstrated that within the RxSM this can only be realized if the mass of the second Higgs boson is not too large, $m_H \lesssim 900$ GeV. For a broad class of models this was shown in Refs. [25, 26]. This makes the boson H a prime target for the HL-LHC, but also for future high-energy e^+e^-

colliders.

The related physics questions are two-fold. Can such a new, heavier Higgs boson, as favored by a FOEWPT, be detected at the HL-LHC and/or high-energy e^+e^- colliders? Can we gain access to BSM THCs through the processes $gg \rightarrow hh$ at the HL-LHC, or $e^+e^- \rightarrow Zhh/\nu\bar{\nu}hh$ at a high-energy e^+e^- collider, via a resonant s -channel heavy Higgs boson exchange, involving the BSM THC λ_{hhH} ?

In our analysis we will assume the RxSM exhibiting a FOEWPT in the early universe as required by EW baryogenesis. Here we make use of Ref. [25] defining a 2-dimensional benchmark plane that allows an analysis where the FOEWPT is ensured. We will furthermore assume that the additional Higgs boson H will have been found at the HL-LHC in single heavy Higgs production. For the HL-LHC we will analyze di-Higgs production, $gg \rightarrow hh$, as evaluated with the code HPAIR Refs. [27, 28], where the H appears as a heavy s -channel resonance, $gg \rightarrow H \rightarrow hh$. Employing the invariant di-Higgs mass distributions, m_{hh} , we will analyze the sensitivity of the HL-LHC to the BSM THC λ_{hhH} . In passing, we will demonstrate that the simplification employed by ATLAS and CMS in the search for resonant di-Higgs production, leaving out the SM-like contributions in the signal model, is highly questionable (see also Ref. [21].)

The analysis is extended to future high-energy e^+e^- colliders, like the ILC [29] and CLIC [30], which can play a key role for the measurement of the Higgs potential with high precision and in detecting possible deviations from the SM [18, 19, 31–34].¹ More specifically, we will analyze the process $e^+e^- \rightarrow ZH \rightarrow Zhh$ at the ILC1000, i.e. a linear collider operating at $\sqrt{s} = 1000$ GeV.² Like for the process $gg \rightarrow hh$ the heavy Higgs can appear as a resonance, involving λ_{hhH} . Employing the m_{hh} distributions we derive the sensitivity to λ_{hhH} at the ILC1000. Similar analyses within the 2HDM, but without the focus on the FOEWPT, can be found in Ref. [20] for the HL-LHC and in Refs. [35, 36] for ILC and CLIC. Further analyses involving BSM triple Higgs couplings can be found in Refs. [17, 19, 37–39].

The RxSM has been analyzed during the last years w.r.t. FOEWPTs and related phenomena. As discussed above, in Ref. [25] the occurrence of a FOEWPT in the RxSM connected to di-Higgs production was analyzed, followed up by a more detailed analysis of the process $hh \rightarrow bb\gamma\gamma$ in Ref. [40]. A similar analysis focusing on the $b\bar{b}ZZ$ final state was presented in Ref. [41]. The interplay of EW baryogenesis with gravitational waves in the RxSM was first analyzed in Ref. [42], see also Refs. [43, 44] for the inclusion of two-loop effects into the evaluation of the FOEWPT. The inclusion of dimension-6 operators on top of a one-loop calculation was analyzed in Ref. [45]. Results for the FOEWPT employing lattice calculations were presented in Refs. [46, 47]. The latter paper also discussed the HL-LHC phenomenology of resonant di-Higgs searches, but taking into account only the resonant H -exchange contribution. The interference effects with the non-resonant diagrams in the RxSM were analyzed in Ref. [48], but without taking into account the possibility of a FOEWPT. Concerning future colliders, the resonant di-Higgs production in the RxSM at e^+e^- colliders was discussed in Ref. [49], but again without taking the FOEWPT into account. A corresponding analysis for

¹Circular colliders such as FCC-ee or CEPC have only very limited sensitivity to the SM-like THC via loop effects in single Higgs production. Furthermore, they do not have sufficient center-of-mass energy to produce a heavy RxSM Higgs-boson resonantly to gain access to λ_{hhH} .

²While we use certain characteristics of the ILC (e.g. foreseen luminosities), our results are valid for any e^+e^- collider operating at the same center-of-mass energy.

a future $\mu^+\mu^-$ collider can be found in Ref. [50]. In contrast to the existing analyses, in this work we combine the requirement of a FOEWPT with the analysis of di-Higgs production at the HL-LHC including all contributing diagrams, as well as the complementary di-Higgs production at future e^+e^- colliders.

Our paper is organized as follows. In Sect. 2 we briefly review the RxSM, fix our notation, and define the benchmark plane featuring a FOEWPT, used later for our investigation, and summarize the constraints that we apply. In Sect. 3 we analyze the possible sensitivity of the di-Higgs production cross section at the (HL-)LHC to λ_{hhH} and discuss the applicability of resonant di-Higgs searches by ATLAS and CMS to specific models such as the RxSM. In Sect. 4 we extend our analysis of the λ_{hhH} to the ILC1000. Our conclusions are given in Sect. 5.

2 The Model and the Constraints

In this section we give a short description of the RxSM to fix our notation. We briefly review the theoretical and experimental constraints. Finally we will define the benchmark plane and the benchmark points for our analysis of the the di-Higgs production at the (HL-)LHC and the ILC.

2.1 The RxSM

The model that is the framework of our analysis, is the real singlet extension of the SM (RxSM), without imposing a Z_2 symmetry (see Refs. [23, 25, 51] for reviews). This Higgs sector extension adds a real singlet field \mathcal{S} to the complex Higgs doublet \mathcal{H} of the SM Higgs Sector. After EWSB the doublet and the singlet fields can be written in the unitary gauge as

$$\mathcal{H} = \begin{pmatrix} 0 \\ \frac{h'+v}{\sqrt{2}} \end{pmatrix}, \quad \mathcal{S} = s + x, \quad (1)$$

where h' and s are two CP even Higgs fields, x is the singlet vev and $v \sim 246$ GeV is the SM vev. The potential is given by,

$$V(\mathcal{H}, \mathcal{S}) = -\mu^2(\mathcal{H}^\dagger\mathcal{H}) + \lambda(\mathcal{H}^\dagger\mathcal{H})^2 + \frac{a_1}{2}(\mathcal{H}^\dagger\mathcal{H})\mathcal{S} + \frac{a_2}{2}(H^\dagger\mathcal{H})\mathcal{S}^2 + \frac{b_2}{2}\mathcal{S}^2 + \frac{b_3}{3}\mathcal{S}^3 + \frac{b_4}{4}\mathcal{S}^4. \quad (2)$$

The new potential has seven Lagrangian parameters, where a_1 and b_3 are allowed since no Z_2 symmetry is imposed. Taking into account the vevs of the doublet and the singlet fields the model has nine free parameters. The number of free parameters can be reduced to seven by using the minimization conditions of the potential,

$$\left. \frac{dV}{dh'} \right|_{h'=0, s=0} = 0, \quad \left. \frac{dV}{ds} \right|_{h'=0, s=0} = 0, \quad (3)$$

which leads to two relations between the Lagrangian parameters,

$$\mu^2 = \lambda v^2 + (a_1 + a_2 x) \frac{x}{2},$$

$$b_2 = -b_3x - b_4x^2 - \frac{a_1v^2}{4x} - \frac{a_2v^2}{2}. \quad (4)$$

Expanding the potential using the definitions in Eq. (1), the mass matrix can be computed as,

$$M^2 = \left(\begin{array}{cc} \frac{d^2V}{dh'^2} & \frac{d^2V}{dh'ds} \\ \frac{d^2V}{dh'ds} & \frac{d^2V}{ds^2} \end{array} \right) \Big|_{h'=0, s=0} \equiv \left(\begin{array}{cc} m_{h'}^2 & m_{h's}^2 \\ m_{h's}^2 & m_s^2 \end{array} \right) = \left(\begin{array}{cc} 2\lambda v^2 & (a_1 + 2a_2x)\frac{v}{2} \\ (a_1 + 2a_2x)\frac{v}{2} & b_3x + 2b_4x^2 - \frac{a_1v^2}{4x} \end{array} \right). \quad (5)$$

To obtain the expressions for the masses of the physical states h and H , the mass matrix has to be diagonalized with the angle θ ,

$$\begin{pmatrix} h \\ H \end{pmatrix} = \begin{pmatrix} \cos\theta & \sin\theta \\ -\sin\theta & \cos\theta \end{pmatrix} \begin{pmatrix} h' \\ s \end{pmatrix}. \quad (6)$$

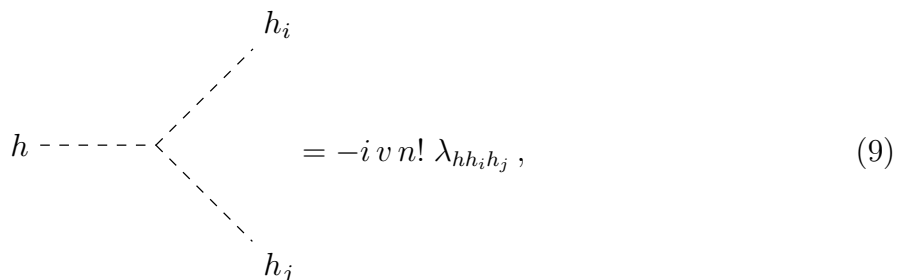
We define h as the lighter state, which we identify with the Higgs boson discovered at the LHC with a mass of ~ 125 GeV. Correspondingly, H is defined as the second, heavier Higgs boson. The physical masses are given by,

$$m_{h,H}^2 = \frac{1}{2} \left(m_{h'}^2 + m_s^2 \mp |m_{h'}^2 - m_s^2| \sqrt{1 + \left(\frac{2m_{h's}^2}{m_{h'}^2 - m_s^2} \right)^2} \right), \quad (7)$$

and the mixing angle by

$$\sin 2\theta = \frac{2m_{h's}^2}{m_H^2 - m_h^2}. \quad (8)$$

The various triple Higgs couplings between the physical fields are obtained from the Higgs potential after rotation to the mass basis and taking the third derivatives with respect to the physical Higgs fields. The triple Higgs couplings $\lambda_{h_i h_j h_k}$ between the physical fields h_i , h_j , and h_k ($h_{i,j,k} \in \{h, H\}$) are defined via the Feynman rule



$$= -i v n! \lambda_{h h_i h_j}, \quad (9)$$

where n is the number of identical particles in the vertex. The following expressions are obtained for the couplings λ_{hhh} between the three SM-like fields h (called SM-like coupling in the following) and λ_{hhH} (called BSM coupling in the following),

$$\lambda_{hhh} = \frac{1}{v} \left[\left(\frac{a_1}{4} + \frac{a_2x}{2} \right) \cos^2\theta \sin\theta + \frac{a_2v}{2} \cos\theta \sin^2\theta + \left(\frac{b_3}{3} + b_4x \right) \sin^3\theta + \lambda v \cos^3\theta \right], \quad (10)$$

$$\lambda_{hhH} = \frac{1}{4v} \left[(a_1 + 2a_2x) \cos^3\theta + 4v(a_2 - 3\lambda) \cos^2\theta \sin\theta \right]$$

$$-2(a_1 + 2a_2x - 2b_3 - 6b_4x) \cos \theta \sin^2 \theta - 2a_2v \sin^3 \theta \Big]. \quad (11)$$

There are two more BSM triple Higgs couplings, involving two or three heavy Higgs bosons, λ_{hHH} and λ_{HHH} . However, they do not play a role in our analysis. The couplings of the Higgs bosons h and H , respectively, to any SM particle i are modified w.r.t. the corresponding SM Higgs-boson coupling $g_{h'i}$. In the RxSM, the couplings are suppressed compared to $g_{h'i}$ by the cosine (sine) of the mixing angle for the light (heavy) Higgs-boson as,

$$g_{hi}^{\text{RxSM}} = g_{h'i}^{\text{SM}} \cdot \cos \theta, \quad g_{Hi}^{\text{RxSM}} = g_{h'i}^{\text{SM}} \cdot \sin \theta. \quad (12)$$

Correspondingly, the decay rates of the RxSM Higgs bosons h and H , respectively, to the SM particles change as

$$\Gamma_{h \rightarrow ii}^{\text{RxSM}} = \Gamma_{H_{\text{SM}} \rightarrow ii} \cdot \cos^2 \theta, \quad \Gamma_{H \rightarrow ii}^{\text{RxSM}} = \Gamma_{H_{\text{SM}} \rightarrow ii} \cdot \sin^2 \theta \quad (13)$$

(with H_{SM} denoting the Higgs boson in the SM, and its mass $m_{H_{\text{SM}}}$ correspondingly set to m_h or m_H in $\Gamma_{H_{\text{SM}} \rightarrow ii}$). The total decay width of the heavy Higgs boson can additionally be modified by the possible decay into two light Higgs-bosons, which (for $m_H > 2m_h$) is given by decay width

$$\Gamma_{H \rightarrow hh} = \frac{\lambda_{hhH}^2}{8\pi m_H} \sqrt{1 - \frac{4m_h^2}{m_H^2}}. \quad (14)$$

The total decay width of the heavy Higgs boson is then calculated as

$$\Gamma_H = \Gamma_{H_{\text{SM}}} \cdot \sin^2 \theta + \Gamma_{H \rightarrow hh}. \quad (15)$$

For $\cos \theta \rightarrow 1$, the light Higgs boson h has the same properties as predicted by the SM with $\Gamma_h = \Gamma_{H_{\text{SM}}}$ (for $m_h = m_{H_{\text{SM}}}$), which is known as the alignment limit. In case of $\cos \theta \rightarrow 0$, H has SM-like couplings and $\Gamma_H = \Gamma_{H_{\text{SM}}}$ for $\Gamma_{H \rightarrow hh} = 0$ (and $m_H = m_{H_{\text{SM}}}$).

Instead of using the original Lagrangian parameters it convenient to employ a more physical parametrization of the RxSM. In this work we use the ‘‘mass basis’’, which includes the masses of the Higgs bosons. It is defined as

$$m_h, m_H, v, x, \theta, a_2, b_4. \quad (16)$$

The transition from the original basis is given by

$$\lambda = \frac{1}{2v^2} (m_H^2 \sin^2 \theta + m_h^2 \cos^2 \theta), \quad (17)$$

$$b_2 = m_h^2 \sin^2 \theta + m_H^2 \cos^2 \theta - \frac{a_2}{2} v^2, \quad (18)$$

$$a_1 = \frac{2}{v} \sin \theta \cos \theta (m_H^2 - m_h^2). \quad (19)$$

Now we can rewrite the triple Higgs couplings as

$$\begin{aligned} \lambda_{hhh} &= \frac{1}{6v^2} \{ 3m_h^2 \cos^5 \theta + 3a_2vx \cos^2 \theta \sin \theta + 3 \cos \theta [a_2v^2 - (m_h^2 - 2m_H^2) \cos^2 \theta] \sin^2 \theta \\ &\quad + 2v(b_3 + 3b_4x) \sin^3 \theta \}, \\ \lambda_{hhH} &= \frac{1}{2v^2} \{ a_2vx \cos^3 \theta + (m_H^2 - 4m_h^2) \sin \theta \cos^4 \theta + \cos^2 \theta [2a_2v^2 \sin \theta \\ &\quad + (2m_h^2 - 5m_H^2) \sin^3 \theta] + v \sin \theta [(b_3 - a_2x + 3b_4x) \sin 2\theta - a_2v \sin^2 \theta] \}. \end{aligned} \quad (20)$$

2.2 Theoretical and Experimental Constraints

In this subsection we briefly summarize the various theoretical and experimental constraints considered in our analysis. It should be noted that we did not check for constraints arising from di-Higgs measurements at the LHC (this will be commented on below, where relevant).

- **Theoretical constraints**

It has to be ensured (we follow Refs. [25, 51]) that the potential is bounded from below and that the couplings are in the perturbative regime. Firstly, for the scalar potential to be stable, the quartic couplings must be positive in all directions of the fields. To ensure this, we demand that the determinant of the Hessian matrix is positive. Second, to ensure perturbative couplings, we require that λ , $\frac{a_2}{2}$ and $\frac{b_4}{4}$ are smaller than 4π . Taking all this into account the following theoretical constraints are found [25]:

$$0 < \lambda, \frac{a_2}{2} \ \& \ \lambda, \frac{a_2}{2}, \frac{b_4}{4} < 4\pi \ \& \ a_2 > -2\sqrt{\lambda b_4}. \quad (21)$$

As will be seen later, phenomenological restrictions even yield $b_4 < 1$. As pointed out in Ref. [25], unitarity constraints do not yield further restrictions on the parameter space beyond Eq. (21).

- **Constraints from direct Higgs-boson searches at colliders**

The exclusion limits at the 95% C.L. of all relevant BSM Higgs boson searches (including Run 2 data from the LHC) are included in the public code `HiggsBounds v.6` [52–57], which is included in the public code `HiggsTools` [57]. For a parameter point in a particular model, `HiggsBounds` determines on the basis of expected limits which is the most sensitive channel to test each BSM Higgs boson. Then, based on this most sensitive channel, `HiggsBounds` determines whether the point is allowed or not at the 95% CL. As input `HiggsBounds` requires some specific predictions from the model, like branching ratios or Higgs-boson couplings (which we evaluate as described in Sect. 2.1).

- **Constraints from the properties of the ~ 125 GeV Higgs boson**

Any model beyond the SM has to accommodate a Higgs boson with mass and signal strengths as they were measured at the LHC. For the parameter points used, the compatibility of the \mathcal{CP} -even scalar h with a mass of 125.09 GeV, h_{125} , with the measurements of signal strengths at the LHC is tested with the code `HiggsSignals v.3` [57–60], which is included in the code `HiggsTools`. The code provides a statistical χ^2 for the h_{125} predictions of a given model in comparison to the measurements of the Higgs-boson signal rates and masses from the LHC. Specifically, we demand that $\chi_{h_{125}, \text{RxSM}}^2 - \chi_{h_{125}, \text{SM}}^2 < 6.3$ (with $\chi_{h_{125}, \text{SM}}^2 = 159.7$).

2.3 Benchmark Plane and Points

After applying the minimization conditions the model has seven free parameters: $a_1, a_2, b_3, b_4, \lambda, v$ and x . Fixing the SM-like Higgs mass m_h and the SM VEV v to their phenomenological values $m_h \approx 125$ GeV and $v \approx 246$ GeV, we are left with five free parameters, a_1, b_3, b_4, λ , and x . The aim in this subsection is to define a benchmark plane with

only two degrees of freedom which features a SFOEWPT, and which maximizes the di-Higgs production cross section at the LHC. The authors of Ref. [25] scanned the RxSM parameter space and kept points exhibiting a SFOEWPT. Out of these they selected eleven points that maximize the di-Higgs production cross section at the LHC, $\sigma(pp \rightarrow H \rightarrow hh)$. We have used these results from Ref. [25] to define our 2-dimensional benchmark plane.

Out of the eleven points provided in Ref. [25] we use eight points which all have $x > 30$ GeV. These points are shown in Tab. 1.³ They approximately fulfill the numerical conditions⁴

$$a_1 x = -32000 , \quad (22)$$

$$\lambda = 0.18 , \quad (23)$$

$$b_3 = -560\sqrt{b_4} , \quad (24)$$

leaving the singlet vev x and the parameter b_4 as our free parameters, so that we arrive at a two-dimensional benchmark plane that features a SFOEWPT. The appearance of “restricted allowed intervals” for the Lagrangian parameters that can be observed in Tab. 1 is just a consequence of the requirement of a SFOEWPT as demanded in Ref. [25].

Benchmark	x [GeV]	λ	a_1 [GeV]	a_2	b_3 [GeV]	b_4	κ_λ	λ_{hhH}
B1	60.9	0.17	-490	2.65	-361	0.52	1.42	0.25
B2	59.6	0.17	-568	3.26	-397	0.78	1.40	0.31
B3	54.6	0.17	-642	3.80	-214	0.16	1.41	0.34
B4	47.4	0.18	-707	4.63	-607	0.85	1.47	0.38
B5	40.7	0.18	-744	5.17	-618	0.82	1.47	0.37
B6	40.5	0.19	-844	5.85	-151	0.08	1.48	0.42
B7	36.4	0.18	-898	7.36	-424	0.28	1.43	0.48
B8	32.9	0.17	-976	8.98	-542	0.53	1.41	0.54

Table 1: Values of x , λ , a_1 , a_2 , b_3 , b_4 , κ_λ , and λ_{hhH} of the reference benchmark points from Ref. [25].

All points of the defined benchmark plane are within the range of parameters that were found to feature a FOEWPT, see our analysis below. Calculating the values of a_1 , λ and b_3 from the values of b_4 and x in Tab. 1 we find a maximum deviation of 7% for a_1 , 6% for λ and 30% for b_3 w.r.t. the values given in Tab. 1. We can use Eq. (4) and Eqs. (17) – (19) to translate the relations in Eq. (24) into the mass basis. This allows us to take into account the experimental and theoretical constraints as described in the previous subsection. The plane is shown in the upper left plot of Fig. 1, where the red stars indicate the eight benchmark points, and the blue points are allowed by all constraints. The gray points are excluded by `HiggsBounds`, which found them to be incompatible with a 2020 ATLAS search for a

³We have checked that these eight points also lead to a FOEWPT using the more updated calculation implemented in `BSMPTv3` [61–63].

⁴For the four points with $x < 30$ GeV the deviations from our three conditions exceed the few-percent level.

resonance of a heavy Higgs boson, which decays into two Z bosons and ultimately into four leptons [64]. This experimental result was not yet available when Ref. [25] was published. We also show the projection of the allowed/excluded regions (blue/grey) in the λ_{hhH} - κ_λ plane in the upper right plot of Fig. 1. It can be seen how almost the entire plane lies in the area defined by the points of [25], which ensures the SFOEWPT in our plane. One can observe that four reference points are outside the plane, because of their smaller or larger value of κ_λ . However, this does not constitute a problem, since the points are outside our benchmark plane by a maximum of 2% in κ_λ . (In Ref. [25] a favorable value of $\kappa_\lambda \sim 1.5$ is found to ensure the SFOEWPT, in agreement with our benchmark plane.) Finally, in the lower plot of Fig. 1 we show a zoom into the allowed regions in the λ_{hhH} - κ_λ plane.

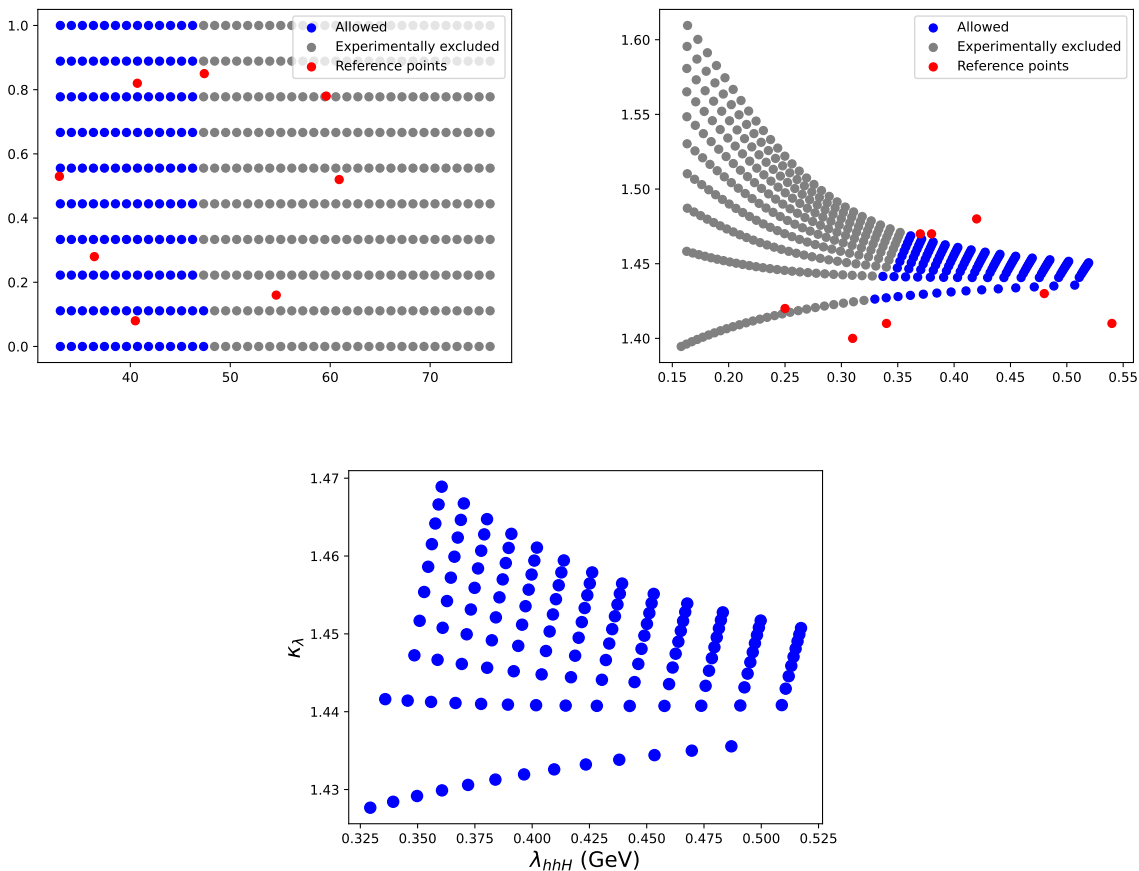


Figure 1: The benchmark plane with the experimentally excluded region in grey, the allowed region in blue and the points used to define the plane in red (see text). Upper left: the prediction in the plane x - b_4 . Upper right: the projection of the benchmark plane in the λ_{hhH} - κ_λ plane. Lower plot: the final allowed benchmark plane in the λ_{hhH} - κ_λ projection.

In the following we briefly analyze the basic phenomenological features of our benchmark plane. In Fig. 2 we show the prediction for m_H in the x - b_4 plane (left) and in the λ_{hhH} - κ_λ plane (right). It can be seen that the mass of the heavy Higgs boson is inversely proportional to the singlet vev. This is an effect of the definition of the benchmark plane, not a feature of the model. The allowed range of m_H in our plane is [458, 660] GeV. One can also see that

λ_{hhH} increases with the heavy Higgs-boson mass. Overall, we find that in our benchmark plane the product of $(\sin \theta \cdot \lambda_{hhH})$ is approximately constant (within a few percent). In the calculation of $gg \rightarrow H \rightarrow hh$ in the limit of large m_H one thus finds a suppression with increasing m_H , and in the limit $m_H \rightarrow \infty$ the amplitude for this process goes to zero.

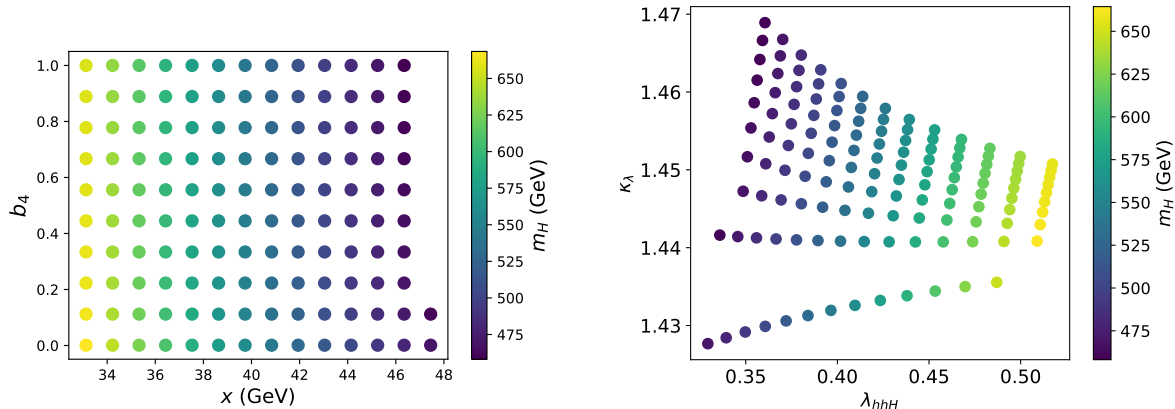


Figure 2: The prediction of the heavy Higgs mass m_H in our benchmark scenario. Left: in the x - b_4 plane, right: in the λ_{hhH} - κ_λ plane.

In Fig. 3 we show the prediction of the mixing angle θ in the x - b_4 plane (left) and in the λ_{hhH} - κ_λ plane (right). The cosine tends to 1 for small values of x , but $\cos \theta = 1$ is never reached, which is again an artifact of our benchmark plane. This is consistent since in the alignment limit the SM is recovered, in which no SFOEWPT is found, whereas it is ensured in our benchmark plane by construction. Similarly, $\kappa_\lambda = 1$ is never reached by construction.

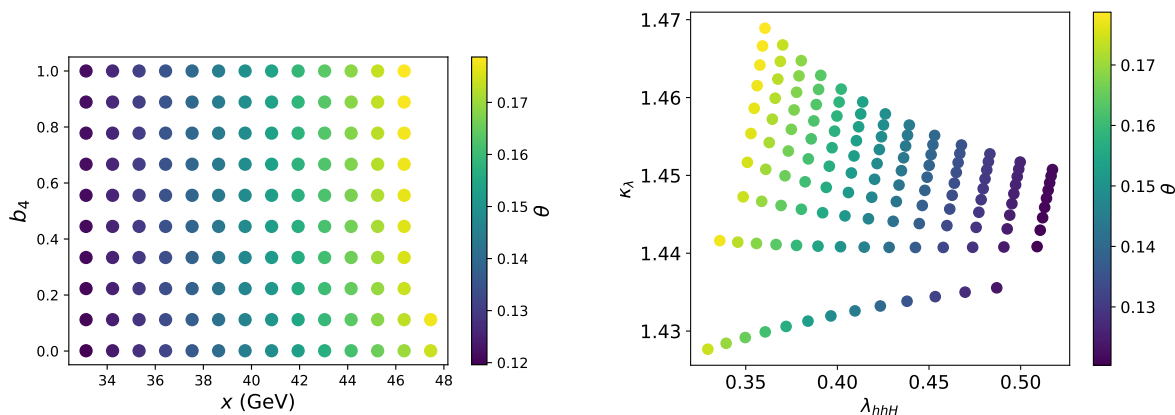


Figure 3: The prediction of the mixing angle in the second benchmark plane. Left: in the $x - b_4$ plane. Right: in the $\lambda_{hhH} - \kappa_\lambda$ plane.

3 The HL-LHC Analysis

In this section, we first briefly review our set-up for the calculation of $pp \rightarrow hh$. We show the results for the cross section in our benchmark plane and analyze whether differences w.r.t. the SM predictions will be observable. Finally, we analyze the sensitivity to the heavy Higgs-boson resonance and its THC, λ_{hhH} . The corresponding analysis for high-energy e^+e^- colliders is presented in the subsequent Sect. 4.

3.1 Calculation of $gg \rightarrow hh$

Standard Model Higgs-pair production has not been observed yet at the LHC, and therefore di-Higgs production constitutes an interesting window to test new physics in future experiments such as the HL-LHC. The main production channel at the (HL-)LHC is gluon fusion. In the SM at leading order (LO), two diagrams contribute to the process: the box diagram (shown by the lower diagram in Fig. 4), which is given by a heavy quark loop with two Yukawa couplings, and the triangle diagram (shown by the upper right diagram in Fig. 4), which is given by a heavy quark loop with a Yukawa coupling and the THC λ_{hhh} .⁵ In the RxSM, an additional diagram contributes: the triangle diagram in which a heavy Higgs boson is propagating in the s -channel (shown by the upper left diagram in Fig. 4). It depends on the Yukawa coupling of the heavy Higgs boson and on the BSM THC λ_{hhH} . The box and the light Higgs triangle diagram are known as the “continuum” or the non-resonant part, while the heavy Higgs triangle diagram is called the “resonant” part (even in the case of $m_H < 2m_h$). It should be noted that in the SM there is a destructive interference between the triangle and the box diagram.

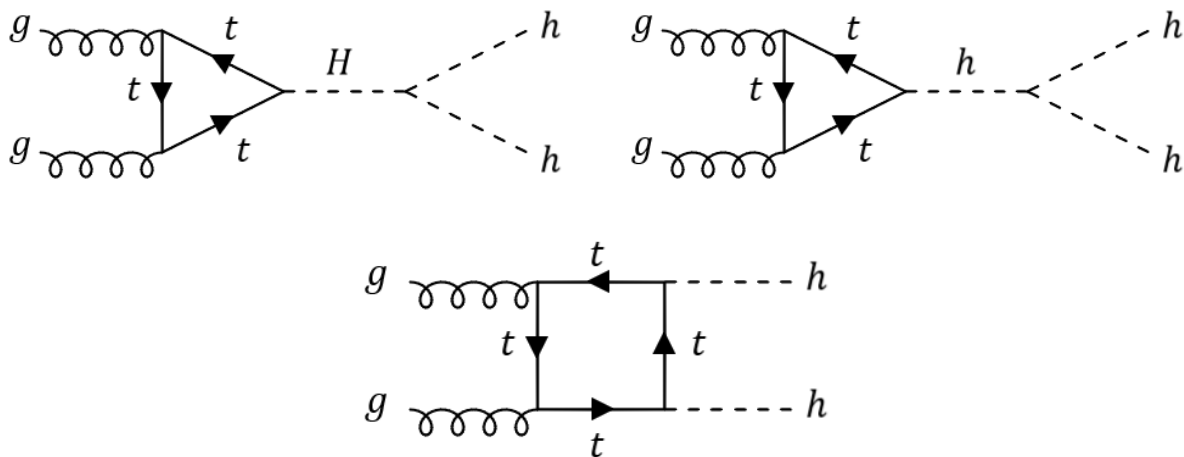


Figure 4: Feynman diagrams entering into the di-Higgs production cross section calculation in the RxSM. Upper left: heavy triangle diagram; upper right: light triangle diagram; down: box diagram.

For our analysis we calculate the total production cross section as well as the differential cross section with respect to the invariant mass of the two light Higgs bosons, m_{hh} . For both

⁵We only display top-quark loops as in the SM the contributions from bottom-loops are very small.

calculations the code `HPAIR` [28] has been used, adapted to the RxSM. The original `Fortran` code `HPAIR` was written to calculate the production cross sections of two neutral Higgs bosons through gluon fusion in the SM and in the Minimal Supersymmetric Extension of the SM (MSSM). In the meantime, it has been extended to other models Refs. [17, 20, 28, 65–67]. For our project, we extended the code to include the RxSM. The computation can be performed either at LO or next-to-leading order (NLO) in QCD. In the LO case, the calculation takes into account the top and bottom quark loops with full mass dependence, whereas in the NLO case the heavy top quark mass limit (HTL) is used. In this limit, the contributions of all quarks are neglected, except for the top quark, which is assumed to be infinitely heavy. The computation of the NLO QCD corrections in the HTL including the full top-quark mass effects at LO leads to a K -factor, i.e. the ratio of the NLO over the LO cross section, of approximately 2 in the SM [28] and also in other BSM extensions, as found in [17, 20, 28, 65–67].⁶ This value approximates the results of the K -factor of the inclusive cross section including the finite top-mass effects at NLO QCD, very well as shown in Refs. [68–72] for the SM and [73, 74] for the 2HDM. The QCD corrections are not affected by Higgs mixings, so they can be taken over to the RxSM case.

The code also provides the calculation of differential cross sections with respect to the invariant Higgs-pair mass, m_{hh} , both at LO and in the HTL. However, as has been shown in Ref. [75] in the context of non-linear effective field theory, mass effects can be significant in the m_{hh} distributions. Since for BSM models there are no results available for distributions at NLO QCD including the full mass dependence, we will stick to LO distributions in the following. Although we are aware that NLO corrections are important, we do not want to present results for distributions that could be significantly distorted by mass effects, and hence chose to make this compromise. Since not all calculations necessary for our analysis can be performed at NLO, we consistently use LO QCD everywhere.

3.2 Analysis of the Cross Section Predictions

In Fig. 5 we show the results for the di-Higgs production cross section in the RxSM at LO. We have verified numerically that the results at NLO QCD are larger by a factor ~ 2 . From now on, we concentrate on the LO result (keeping in mind the NLO factor). All cross section calculations are done for $\sqrt{s} = 14$ TeV. The corresponding SM cross section is obtained with our RxSM version of `HPAIR` setting the mixing angle $\theta = 0$, i.e. in the SM limit. Numerically, we find

$$\sigma_{\text{SM}}^{\text{LO}}(pp \rightarrow hh) = 19.76 \text{ fb}, \quad \sigma_{\text{SM}}^{\text{NLO}}(pp \rightarrow hh) = 38.24 \text{ fb}. \quad (25)$$

In a first step, we compare the results of the RxSM with the SM model ones at the HL-LHC and analyze whether the cross sections of both models can be distinguished experimentally. To do so we define the statistical significance of the RxSM cross section w.r.t. the SM. To calculate the uncertainty of the cross section measurement at the HL-LHC we take the anticipated significance of the SM di-Higgs production cross section at the HL-LHC [76], which has been found to be $s_{\text{SM}} = 4.5\sigma$. This significance is rescaled to the cross section of the RxSM (as the number of expected events will be different). Since we are dealing with a

⁶In our calculations performed for this work we confirmed a K -factor of ~ 2 for the RxSM, see the next subsection.

Gaussian distribution, the uncertainty scales as the square root of the number of events, or in this case of the cross section. The uncertainty $\Delta\sigma_{hh}^{\text{RxSM}}$ on the cross section in the RxSM can then be obtained as,⁷

$$\Delta\sigma_{hh}^{\text{RxSM}} = \frac{\sigma_{hh}^{\text{SM}}}{s_{\text{SM}}} \sqrt{\frac{\sigma_{hh}^{\text{SM}}}{\sigma_{hh}^{\text{RxSM}}}}, \quad (26)$$

and the significance of the deviation of the total RxSM di-Higgs production from the SM prediction is defined as,

$$\Delta s = \frac{\sigma_{hh}^{\text{RxSM}} - \sigma_{hh}^{\text{SM}}}{\Delta\sigma_{hh}^{\text{RxSM}}}. \quad (27)$$

In Fig. 5 we show the $\lambda_{hhH}-\kappa_\lambda$ benchmark plane as defined in the previous section. In the left plot we display as color coding the total cross section of the di-Higgs production in the RxSM and we mark in red when the value of the cross-section in the RxSM is approximately equal to the SM, which we define through the right plot, where we show as color coding the significance of the deviation from the SM, i.e. Δs as defined in Eq. (27), where red points have $|\Delta s < 0.1|$. For values of $\lambda_{hhH} \lesssim 0.4255$ we find larger RxSM cross section values than in the SM, whereas for larger λ_{hhH} values they are smaller. However, this is not a general feature, but an artifact of our benchmark plane. The figure shows that the cross-section of the process is inversely proportional to the THC λ_{hhH} . Here it is important to keep in mind that λ_{hhH} increases with m_H . However, as argued in the section where the benchmark plane is defined, an overall suppression of the heavy Higgs-boson contribution is expected with increasing λ_{hhH} due to the fact that in our benchmark plane we find that the product of $(\sin\theta \cdot \lambda_{hhH})$ is approximately constant. Finally, as can be observed in the right plot of Fig. 5, we find that for the smallest allowed values of λ_{hhH} in our benchmark plane the cross section of the RxSM deviates by more than 3σ from the SM prediction, i.e. from the cross section measurement alone a difference could be observed. For most parts of the parameter space, however, this difference is too small to be significant.

In the region where $\sigma_{hh}^{\text{SM}} \approx \sigma_{hh}^{\text{RxSM}}$, i.e. the region marked in red in the right plot of Fig. 5, the RxSM is not in the alignment limit, but the various BSM effects cancel each other. W.r.t. the SM one has $\kappa_\lambda \sim 1.45$, i.e. the destructive interference of the box diagram and the h s -channel contribution is enhanced, leading to a smaller cross section. This, however, is compensated by the resonant H exchange contribution, leading to an accidental numerical cancellation of both effects.

Resonant di-Higgs-boson searches at ATLAS Refs. [15, 77] and CMS Refs. [16, 78] so far take into account only the resonant diagram, but neglect possible effects from the two continuum diagrams, which will be discussed further in Sect. 3.3. Here, in Fig. 6, we show the total cross section in the RxSM for the case that the continuum diagrams are (incorrectly) not taken into account. It can be observed that this cross section is lower than the SM result by $\sim 20\%$ for small values of λ_{hhH} and by up to $\sim 80\%$ for large values of λ_{hhH} . These numbers differ substantially from the complete calculation taking into account all diagrams, as shown in Fig. 5. This demonstrates already at the level of the full cross section that the

⁷Since, as discussed above, also in the RxSM the K -factor is ~ 2 as in the SM, we can safely assume that the NLO QCD corrections, that are not taken into account (see the discussion above), rescale all cross sections and the corresponding uncertainties in the same way.

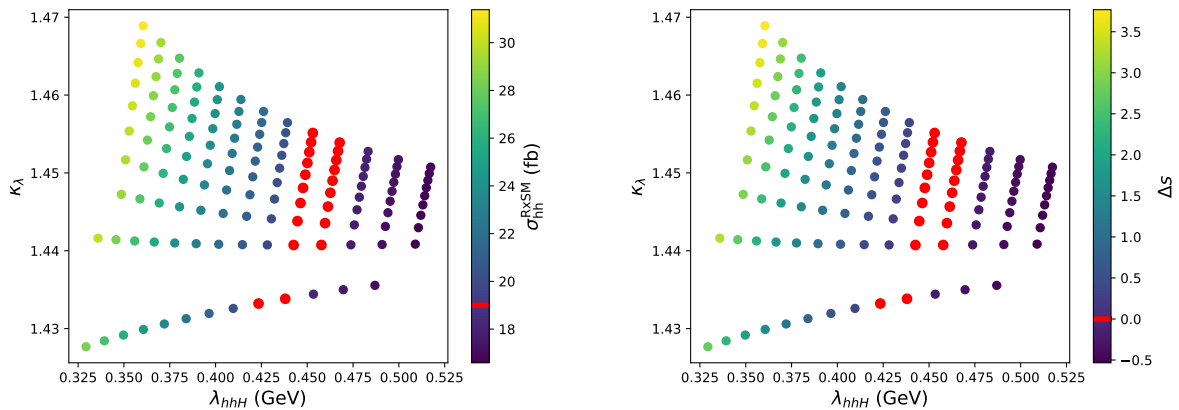


Figure 5: The λ_{hhH} - κ_λ benchmark plane. Left: total cross section of the process $gg \rightarrow hh$ for the HL-LHC in the RxSM. The red mark on the colorbar corresponds to $\sigma_{hh}^{\text{RxSM}} = \sigma_{hh}^{\text{SM}}$. The red colored points are defined via the right plot (see text). Right: the significance of the cross section of the process $gg \rightarrow hh$ in the RxSM w.r.t. the SM. The red mark on the colorbar corresponds to $\Delta s = 0$, and the red points have $|\Delta s| < 0.1$.

experimental “approximation” of neglecting the continuum diagrams may not be adequate in all cases.

3.3 Analysis of m_{hh}

3.3.1 Definitions and Benchmark Points

Experimental di-Higgs analyses not only rely on the total cross section, but also build substantially on differential distributions like the differential invariant mass distribution of the di-Higgs system, m_{hh} (which we evaluate, as discussed above, also with the code `HPAIR`). This will be particularly relevant in parameter regions where $\Delta s < 3$, i.e. the measurement of the total cross section is not sufficient to distinguish the RxSM from the SM. To facilitate our analysis, we are going to focus on eight benchmark points distributed over the plane. They have been selected to explore parameter regions with different values of the BSM Higgs-boson mass, different couplings and also different values of the statistical significance of the total cross section with respect to the SM. The eight benchmark points that we have defined are shown in Fig. 7, with their input parameters and other relevant quantities given in Tab. 2. In our analysis we will group these benchmark points according to the differences between $\sigma_{hh}^{\text{RxSM}}$ and σ_{hh}^{SM} in each point. Specifically, we define

- **Region 1:** $\Delta s > 3$,
- **Region 2:** $3 > \Delta s > 0.5$,
- **Region 3:** $0.5 > \Delta s > -0.5$.

Before we present our m_{hh} analysis, we discuss the impact of the experimental uncertainties, see Ref. [20]. In Fig. 8 we show the theoretical prediction for the m_{hh} distribution in black

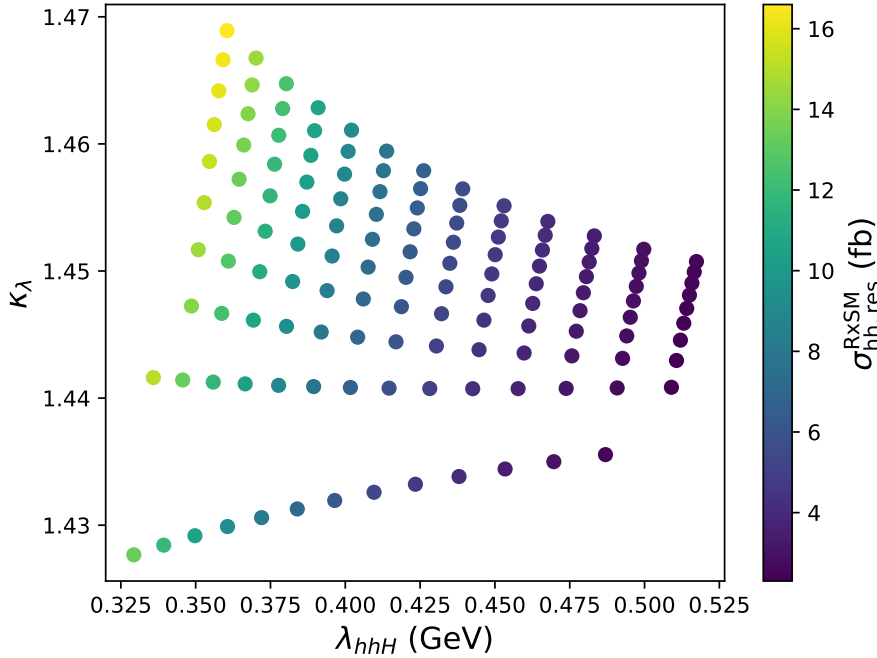


Figure 6: The cross section of the process $gg \rightarrow hh$ for the HL-LHC in the RxSM only taking into account the heavy Higgs boson triangle diagram, shown in the plane λ_{hhH} - κ_λ .

Id	m_H [GeV]	θ	x [GeV]	b_4	λ_{hhH}	κ_λ	Γ_H [GeV]	$\sigma_{hh}^{\text{RxSM}}$ [fb]	Δs	R
P1	459.2	0.178	46.3	0.89	0.36	1.47	3.81	31.1	3.7	235
P2	464.9	0.176	46.3	0.45	0.35	1.46	3.73	30.0	3.2	224
P3	469.4	0.174	47.4	0.00	0.32	1.43	3.48	28.4	2.7	206
P4	529.8	0.153	41.9	0.00	0.38	1.43	4.15	23.3	1.1	158
P5	577.5	0.139	37.5	0.78	0.45	1.45	5.05	19.5	0.1	111
P6	531.7	0.152	40.8	0.45	0.40	1.45	4.49	22.4	0.9	146
P7	642.9	0.125	34.2	0.11	0.49	1.44	5.5	17.5	-0.3	80
P8	657.9	0.122	33.1	0.78	0.52	1.44	5.84	17.3	-0.4	76

Table 2: Benchmark points: identifier, heavy Higgs mass, mixing angle, singlet vev, b_4 , λ_{hhH} coupling, κ_λ modifier, heavy Higgs decay width, di-Higgs production cross section at the HL-LHC, Δs , and the R parameter defined in Eq. (28), see text.

for the benchmark point P1, as given in Tab. 2. It has a dip for low values of the invariant mass, $m_{hh} \sim 290$ GeV. This is caused by a negative interference between the box and the light Higgs-boson triangle diagrams. In the SM with $\kappa_\lambda \sim 1$ this interference occurs at $m_{hh} \sim 250$ GeV. In P1 we have $\kappa_\lambda \sim 1.5$, and the negative interference is shifted to $m_{hh} \sim 290$ GeV. The second important effect is the peak-dip structure observed around the

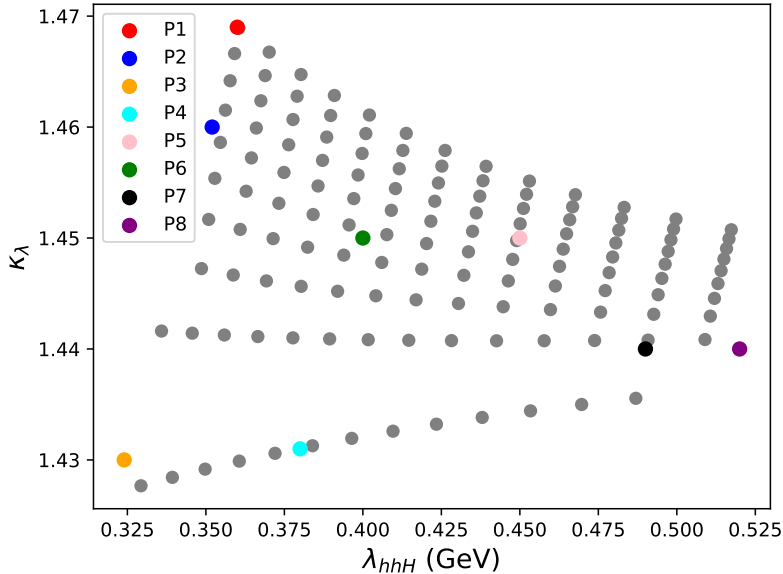


Figure 7: The λ_{hhH} - κ_λ plane with the eight benchmark points marked. For details, see Tab. 2.

resonance of the heavy Higgs boson, $m_{hh} = m_H \sim 460$ GeV. This peak-dip structure is due to the interference of the heavy Higgs-boson triangle and the two non-resonant diagrams, see the discussion in Ref. [20] and references therein. The sign of the couplings entering the heavy Higgs-boson resonance diagram, $Y_t \cdot \lambda_{hhH}$, where Y_t is the top Yukawa coupling of the heavy Higgs boson, determines whether one finds a peak-dip structure (as in our case), or a dip-peak structure.

The first experimental uncertainty that has to be taken into account is the uncertainty in the m_{hh} measurement, labeled as “smearing”. Here we follow the procedure of Ref. [20], where each point in m_{hh} is smeared out as a Gaussian distribution in m_{hh} . We represent each point in m_{hh} as a Gaussian distribution with a full width half maximum (FWHM) of a percentage (p) of the corresponding value of m_{hh} , see Ref. [20] for details, where it was argued that the percentage (p) value to perform a realistic analysis is 15%. The effect of smearing on a distribution can be seen in the blue curve in Fig. 8. It can be observed how the distribution is smoothened out and does not exhibit a pronounced peak-dip structure anymore, which will make it more difficult to identify the resonance contribution. The second effect to be taken into account is that the detector does not have an infinite resolution in m_{hh} . Instead, the data will be given in bins of 50 GeV width, see again the discussion in Ref. [20]. Taking this into account on top of the smearing results in the red curve shown in Fig. 8. Identifying the resonance contribution becomes even more difficult taking the finite resolution in m_{hh} into account.

One main objective of our analysis is the question whether we can distinguish the RxSM from the SM via the m_{hh} distributions, i.e. whether the effect of the heavy Higgs-boson resonance can be detected. To this end, we define a theoretical parameter, R , to compare quantitatively the difference between the RxSM and the SM distributions for the different

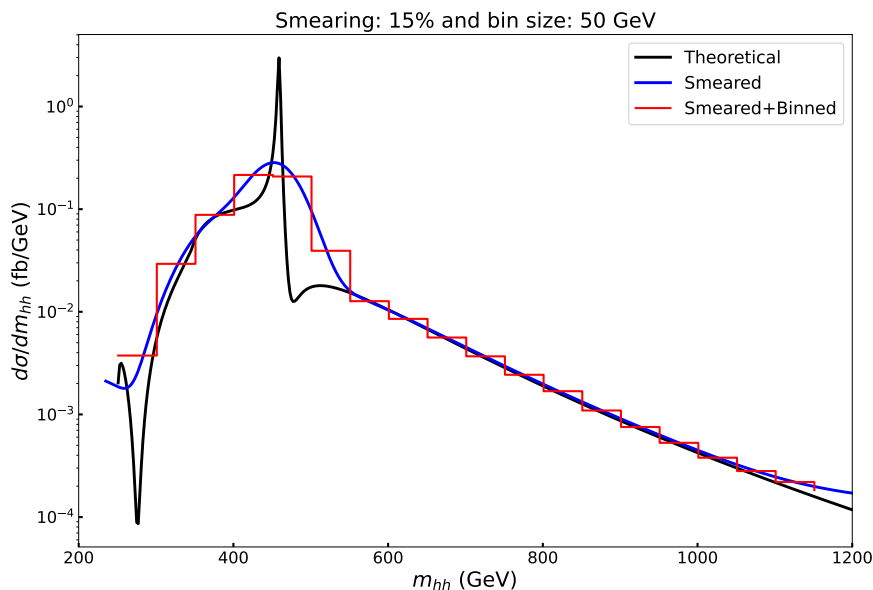


Figure 8: Differential cross section of the process $pp \rightarrow hh$ at the HL-LHC with $\sqrt{s} = 14$ GeV as a function of m_{hh} for the point P1, see Tab. 2; black: theoretical curve, blue: smeared curve with 15% of smearing, red: smeared and binned curve with 15% of smearing and a bin size of 50 GeV.

benchmark points. Following Ref. [20], we define R as,

$$R = \frac{\sum_i |N_i^R - N_i^C|}{\sqrt{\sum_i N_i^C}}, \quad (28)$$

where N_i^R is the number of events of the RxSM distribution, and N_i^C is the number of events of the SM distribution in bin i . The window in which the bins are counted is defined by [20],

$$|N^R - N^C| > \text{bin size} \cdot 20 \text{ GeV}, \quad (29)$$

i.e., the sum over i in Eq. (28) runs over all the bins that fulfill the condition in Eq. (29). With this choice we focus on the region in which there are sizeable differences between the two distributions, i.e. around the resonance. It is important to emphasize that R is a theoretical measure to compare the two distributions with each other. To determine whether via an m_{hh} distribution the measurement the value of the THC λ_{hhH} can be performed, a full experimental analysis is required, which is beyond the scope of this paper.

3.3.2 Complete Calculation

In this subsection we present our results for the calculation of the differential cross section based on the full set of LO diagrams. In the next subsection we highlight the differences w.r.t. the calculation taking into account only the resonant heavy Higgs-boson diagram, as done by the experimental collaborations to obtain their exclusion limits.

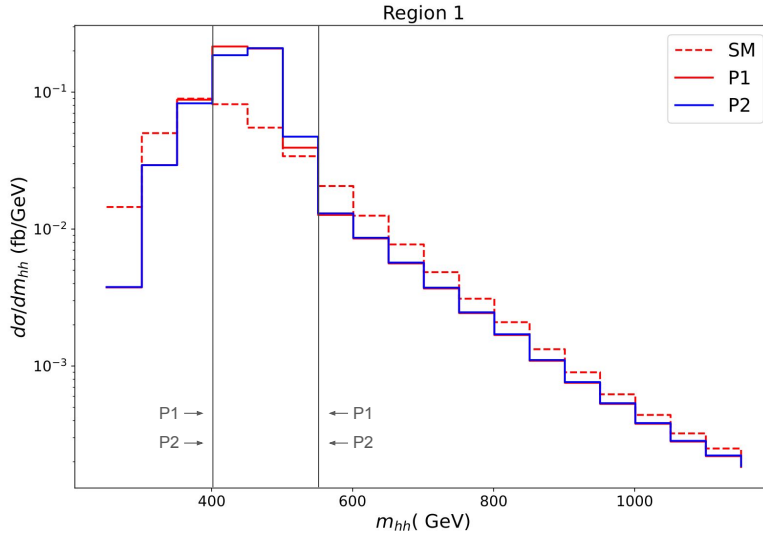


Figure 9: Differential cross section of the process $pp \rightarrow hh$ at the HL-LHC as a function of m_{hh} for the SM (red dashed line) and for two RxSM benchmark points: P1 (red) and P2 (blue), see Tab. 2. Results are shown for a smearing of 15% and a bin size of 50 GeV. The bins that have been used to calculate the R values are indicated by gray vertical lines.

Region 1

In the first region with $\Delta s > 3$ one could observe indications of BSM physics via the total cross-section measurement alone. Two benchmark points, P1 and P2, lie in Region 1. In Fig. 9 we show the m_{hh} distributions for a smearing of 15% and a bin size of 50 GeV, as discussed in the previous subsection. Compared are the results for the SM (red dashed line), benchmark point P1 (red) and P2 (blue). One can observe that the “original” dip-peak structure, as e.g. visible in Fig. 8, is not visible anymore, an effect of the smearing and binning. On the other hand, a pronounced peak w.r.t. the SM is visible around $m_{hh} \sim 460$ GeV, which corresponds to a good approximation to the values of m_H in P1 and P2. The values found for R according to Eqs. (28) and (29) are $R \sim 230$ (see also Tab. 2), where we have indicated in Fig. 9, which bins are taken into account in the respective evaluation. While R is not representing a true experimental significance, the values are relatively high, giving rise to the expectation that the RxSM and the SM can be distinguished not only via a measurement of the total cross section, but also via a measurement of the m_{hh} distributions.

Region 2

In the second region the difference in the total di-Higgs production cross section between the RxSM and the SM is $3 > \Delta s > 0.5$, i.e. the total cross section measurement would not exhibit a significant deviation. However, as discussed above, this is due to the cancelation of several BSM effects, as we will demonstrate here. In Fig. 10 we show the m_{hh} distributions of the three benchmark points in region 2, P3 (orange), P4 (cyan) and P6 (pink), see Tab. 2. As before, they are compared to the SM distribution (dashed red), and a smearing of 15% and a bin size of 50 GeV have been applied. As for region 1, it can be observed how the

peak-dip structure is washed out, leaving resonance peaks around the values of m_H , with $m_H \sim 470$ GeV for P3 and $m_H \sim 530$ GeV for P4 and P6 (see also Tab. 2), where we have indicated in Fig. 10, which bins are taken into account in the respective evaluation. Most importantly, all three RxSM distributions differ substantially from the SM m_{hh} distribution where the differential cross section is large. The values of R found for the three points are ~ 200 for P3, and ~ 150 for P4 and P6. These large values give rise to the hope that while the total cross section does not allow to distinguish the RxSM from the SM, such a distinction may be possible via the measurement of the m_{hh} distribution in comparison with the theory prediction for the SM.

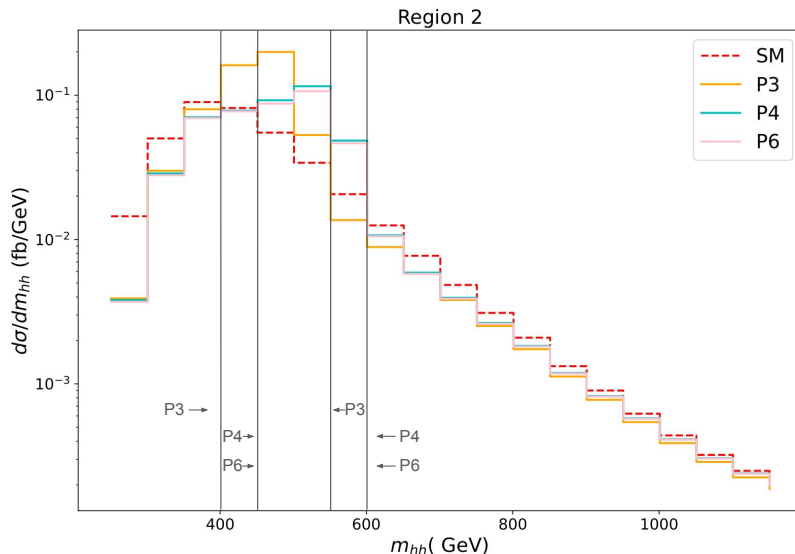


Figure 10: Differential cross section of the process $pp \rightarrow hh$ at the HL-LHC as a function of m_{hh} for the SM (red dashed line) and for three RxSM benchmark points in region 2: P3 (orange), P4 (cyan) and P6 (pink), see Tab. 2. Results are shown for a smearing of 15% and a bin size of 50 GeV. The bins that have been used to calculate the R values are indicated with grey lines.

Region 3

In the third region the difference in the total di-Higgs production cross section between the RxSM and the SM is $0.5 > \Delta_s > -0.5$, i.e. the total cross section in the RxSM is effectively identical to the SM prediction. In Fig. 11 we show the m_{hh} distributions of the three benchmark points in region 3, P5 (green), P7 (purple) and P8 (black), see Tab. 2. As before, they are compared to the SM distribution (dashed red), and a smearing of 15% and a bin size of 50 GeV have been applied. From the original peak-dip structure only a broadly smeared out “resonance peak” remains, again centered around the respective values of the heavy Higgs-boson mass. However, in contrast to regions 1 and 2, the differences w.r.t. the SM m_{hh} distribution around m_H , i.e. where the differential cross section is relatively large, appears much smaller than in the regions 1 and 2. Correspondingly, relatively smaller R values are found: $R \sim 110$ for P5, and $R \sim 80$ for P7 and P8 (see also Tab. 2), where again we have indicated in Fig. 11, which bins are taken into account in the respective evaluation. While these values still appear substantial, a more realistic experimental analysis will be

needed to determine whether in region 3 the m_{hh} measurement at the HL-LHC will be able to distinguish the RxSM from the SM.

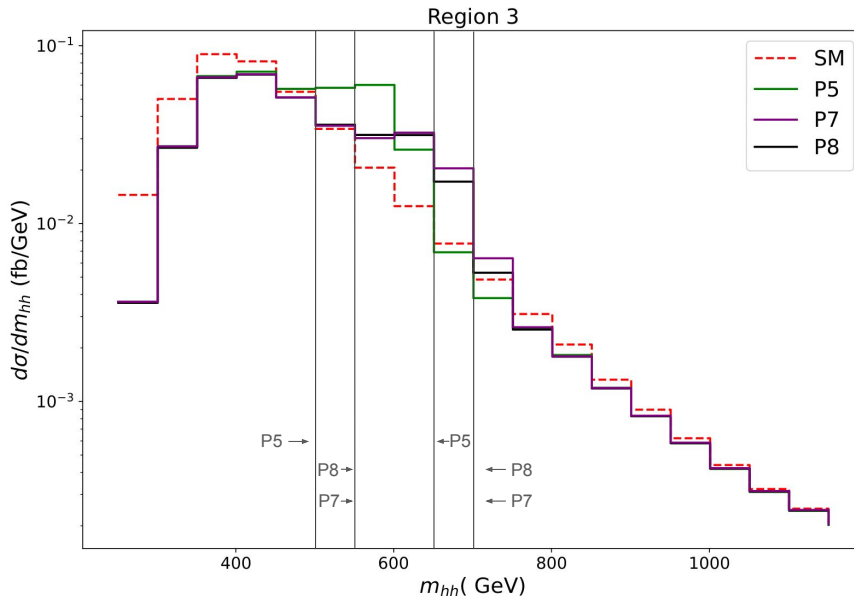


Figure 11: Differential cross section of the process $pp \rightarrow hh$ at the HL-LHC as a function of m_{hh} for the SM (red dashed line) and for three RxSM benchmark points in region 3: P5 (green), P7 (purple) and P8 (black), see Tab. 2. Results are shown for a smearing of 15% and a bin size of 50 GeV. The bins that have been used to calculate the R values are indicated with gray lines.

3.3.3 Pure Heavy Resonant Contribution

In view of recent improvements in the experimental sensitivity to resonant di-Higgs production (see, e.g., Refs. [15,16]) it is crucial that the experimental limits (and possibly eventually also the experimental measurements) are presented in a way that they can be correctly confronted with theoretical predictions in different models. The resonant limits that have been presented by ATLAS [15] and CMS [16] so far were obtained assuming that only one heavy resonance is contributing to the cross section, neglecting the non-resonant contributions. In Ref. [21] it was demonstrated for benchmark points in the 2HDM that the current experimental procedure may not yield reliable resonant di-Higgs exclusion limits. In this subsection we compare the m_{hh} distributions of the full calculation, as presented in the previous subsection, with the distributions obtained neglecting the non-resonant contributions, i.e. m_{hh} distributions of the type employed by the experimental collaborations to obtain their current exclusion bounds. The comparison is shown for one benchmark point in each region.

In Fig. 12 we show the differential cross section of the process $pp \rightarrow hh$ at the HL-LHC as a function of m_{hh} for the SM (red dashed line), compared to the distributions in P1 (region 1, upper plot), P4 (region 2, middle plot) and P7 (region 3, lower plot), see Tab. 2. Orange (blue) lines show the result of the full calculation (taking into account only the resonant diagram). For all three depicted benchmark points the pure resonant m_{hh} distribution exhibits, as expected, a clear peak structure around the respective $m_{hh} = m_H$ value. The correct m_{hh} distributions, i.e. taking correctly into account the resonant contribution, the non-resonant

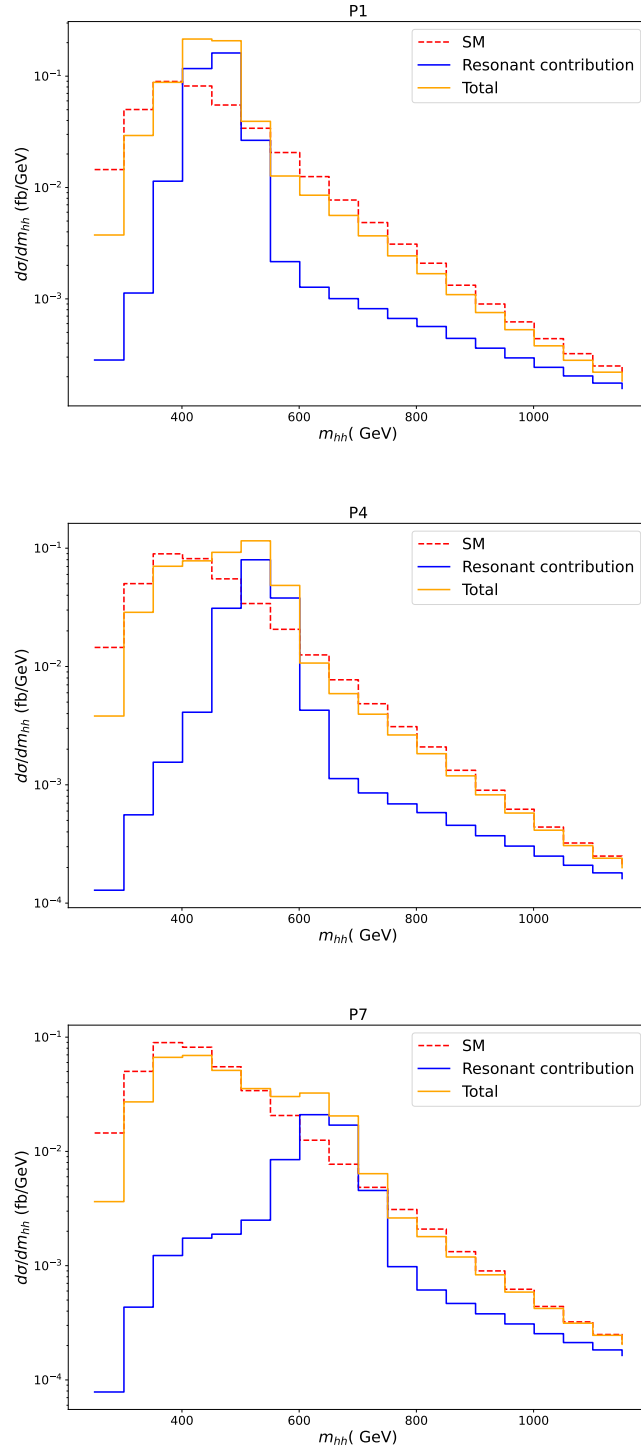


Figure 12: Differential cross section of the process $pp \rightarrow hh$ at the HL-LHC as a function of m_{hh} for the SM (red dashed line), compared to the distributions in P1 (region 1, upper plot), P4 (region 2, middle plot) and P7 (region 3, lower plot), see Tab. 2. Orange (blue) lines show the result of the full calculation (taking into account only the resonant diagram).

diagrams, as well as all interference contributions, have a substantially broader structure. For $m_{hh} \gtrsim m_H$ the m_{hh} distributions are somewhat enhanced w.r.t. the pure resonant result. However, substantially larger effects of the correct full calculation are found for $m_{hh} \lesssim m_H$. In P1 (region 1) the resonant peak is somewhat broadened to smaller m_{hh} values. For P4 (region 2) the peak is broadened already over several bins towards smaller m_{hh} values, where the effect becomes most pronounced for P7 (region 3). As argued in Ref. [21], it is plausible to conclude that such (realistically) broadened peak structures, deviating strongly from the clear peak structure of the pure resonant contribution, could not be identified by the current design of the experimental searches. Conversely, applying a pure resonant m_{hh} distribution to the experimental analysis could lead to an erroneous exclusion of a parameter point, which in reality produces a substantially broadened m_{hh} “peak structure”.

4 ILC1000 Results

In this section we present our results for the di-Higgs production at future high-energy e^+e^- colliders. We consider the double Higgs-strahlung channel, i.e. $e^+e^- \rightarrow Zhhh$, which is the dominant production channel of two SM-like Higgs bosons up to a center-of-mass energy slightly above 1 TeV. The Feynman diagrams that contribute to this process at tree level are shown in Fig. 13. In particular, our study focuses on the effects induced by the two upper diagrams, since these are the ones containing the triple Higgs couplings λ_{hhh} (upper left) and λ_{hhH} (upper right diagram).

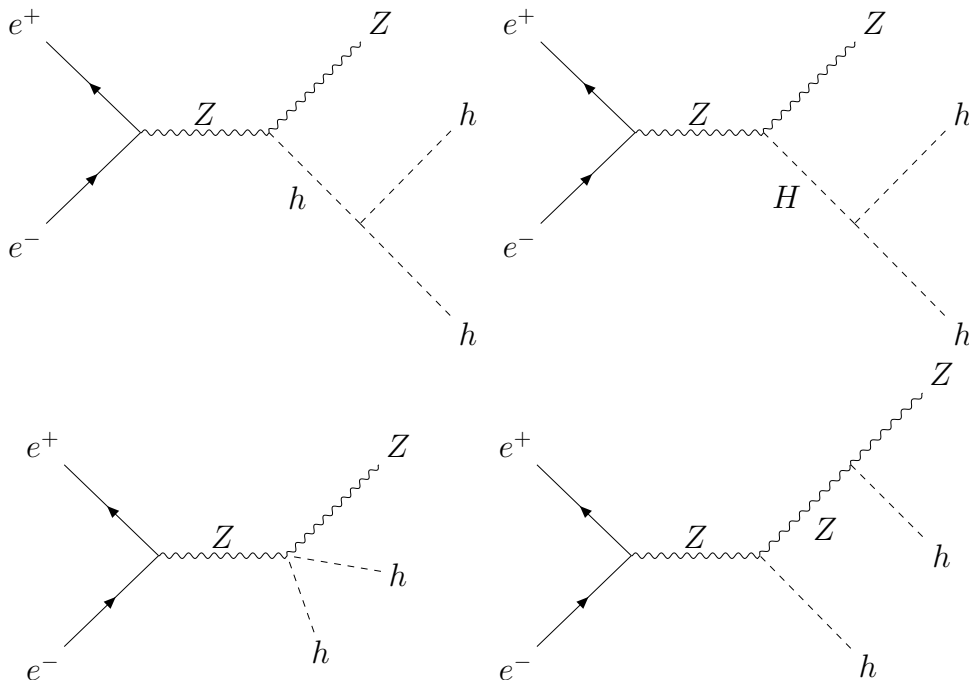


Figure 13: Generic Feynman diagrams contributing to the double Higgs-strahlung process $e^+e^- \rightarrow Zhhh$ in the RxSM.

Similarly to the previous HL-LHC study, we employ the differential cross section distributions of the invariant mass of the final state Higgs-boson pair, m_{hh} , to study the effects of the two THCs involved in the cross section prediction. The contributions proportional to λ_{hhh} enter via a non-resonant diagram, similar to the SM case. Correspondingly, the largest effects of λ_{hhh} are expected at low values of m_{hh} , close to the kinematic threshold. On the other hand, the contributions proportional to the BSM THC, λ_{hhH} , enter via a (potentially) resonant diagram mediated by the heavy Higgs boson H . Therefore, the sensitivity to λ_{hhH} could be accessed by detecting a resonance structure in the invariant mass distribution around $m_{hh} = m_H$.

4.1 Calculation of $e^+e^- \rightarrow Zhh$

We compute the unpolarized cross section for the double Higgs-strahlung process at the tree-level with the help of the public code `Madgraph5_aMC v3.5.7` [79]. The input model file of the RxSM required by `Madgraph` was obtained with the `Mathematica` package `SARAH-4.15` [80]. We compute the cross section for the ILC operating at a center-of-mass energy of $\sqrt{s} = 1000$ GeV (ILC1000) [29, 81, 82]. The choice for the large center-of-mass energy is due to the large values of m_H in our selected benchmark points, see Tab. 2. In this work we assume an integrated luminosity of 8 ab^{-1} , as projected for the ILC1000 [29] (neglecting the possibility of polarized beams).

Using our computational setup, we obtain a prediction for $\sigma(e^+e^- \rightarrow Zhh)$ of 0.12 fb in the SM for a center-of-mass energy of 1 TeV. At $\sqrt{s} = 500$ GeV we find $\sigma(e^+e^- \rightarrow Zhh) = 0.16$ fb. For this center-of-mass energy it is expected to have a discovery of the di-Higgs-strahlung process at the 8σ level for an integrated luminosity of 4 ab^{-1} (combining several polarization runs), corresponding to an experimental uncertainty of 16.8% [83]. Applying a simple scaling with the number of events, this yields a relative uncertainty of the cross section at $\sqrt{s} = 1000$ GeV of $\sim 10\%$ for an integrated luminosity of 8 ab^{-1} , which corresponds to a significance of close to 13σ .

In Fig. 14 we show the prediction of $\sigma(e^+e^- \rightarrow Zhh)$ in the RxSM in the $\lambda_{hhH}-\kappa_\lambda$ benchmark plane, see Sect. 2.3. It ranges from ~ 0.148 fb for smaller κ_λ and larger λ_{hhH} , up to ~ 0.173 fb for larger κ_λ and smaller λ_{hhH} . Rescaling the expected precision with the enhanced cross section in the RxSM w.r.t. the SM prediction, this yields a difference of the RxSM prediction in our benchmark plane between $\sim 2\sigma$ up to $\sim 4\sigma$ w.r.t. the SM applying Eq. (27), but in the case of an e^+e^- collider). Another observation can be made for the contribution of the heavy Higgs-boson resonance. The size of the H -resonance contribution becomes smaller with increasing λ_{hhH} . The reason behind is the fact that in our benchmark plane the product of $(\sin\theta \cdot \lambda_{hhH})$ is approximately constant. Larger λ_{hhH} , however, corresponds to larger m_H , leading to an overall suppression of $\sigma(e^+e^- \rightarrow ZH) \times \text{BR}(H \rightarrow hh)$ for larger λ_{hhH} , as can be seen in the blue curves in Figs. 15 and 16 below. On the other hand, the cross section leaving out the H -resonance contribution remains nearly constant over the plane, as can be observed in the green curves in Figs. 15 and 16, below. In combination with the corresponding interference effects, the overall contribution of the heavy Higgs-boson resonance to the total cross section decreases with increasing λ_{hhH} , leading to smaller $\sigma(e^+e^- \rightarrow Zhh)$ for larger λ_{hhH} as observed in Fig. 14. A more detailed analysis of the THC dependencies will be given in the next subsection. But it is interesting to note that a

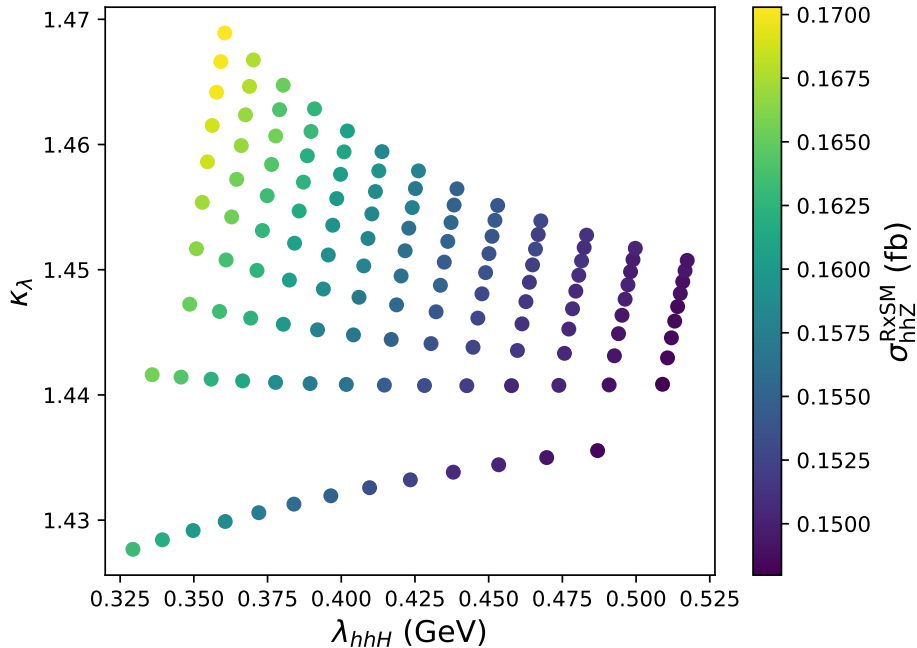


Figure 14: κ_λ - λ_{hhH} plane as a function of the total cross section for the process $e^+e^- \rightarrow ZhH$ at the ILC1000 in our benchmark plane.

parameter space of the RxSM that was identified to yield a strong FOEWPT and is favorable for the di-Higgs production at the LHC [25] yields possibly detectable deviations from the SM also at e^+e^- colliders.

While we also comment on the effects of λ_{hhh} on the total and the differential cross sections in the next subsection, a major focus of this work is to study the potential sensitivity of the ILC1000 to the THC, λ_{hhH} , via an analysis of the H resonance structure. In order to take into account in more detail the experimental analyses (i.e. detector effects, cuts, etc.) we focus on the main light Higgs-boson decay channel, $h \rightarrow b\bar{b}$, which in the SM has a BR of ~ 0.58 . Consequently, the main experimental signature is given by four b -quark jets together with a Z boson. Therefore, following a similar strategy as in Ref. [35], we estimate the expected number of events with four b jets and one Z boson, denoted by \bar{N} , that could be detected at the ILC1000 with the following expression:

$$\bar{N} = N \times (\text{BR}(h \rightarrow b\bar{b}))^2 \times \mathcal{A} \times \epsilon_b^4, \quad (30)$$

where N is the inclusive number of Zhh events predicted by the RxSM, as calculated above. We assume a conservative b -tagging efficiency of $\epsilon_b = 80\%$ for each final b -jet. We also assume the SM prediction for the $h \rightarrow b\bar{b}$ branching ratio (in good agreement with the LHC measurements). \mathcal{A} is our estimation of the detector acceptance after applying the following pre-selection cuts to detect the final $4b + Z$ events (see Ref. [35] for details):

$$p_T^Z > 20 \text{ GeV}, \quad p_T^b > 20 \text{ GeV}, \quad |\eta_b| < 2, \quad \Delta R_{bb} > 0.4, \quad (31)$$

where p_T^Z and p_T^b are the transverse momenta of the Z boson and each of the b quarks, respectively, η_b is the pseudo-rapidity of each of the b quarks, and ΔR_{bb} is the angular separation between two b quarks defined by $\Delta R_{ij} = \sqrt{(\eta_i - \eta_j)^2 + (\phi_i - \phi_j)^2}$, with ϕ being the azimuthal angle. We compute the acceptance \mathcal{A} by simulating the process $e^+e^- \rightarrow Zhh$ with the subsequent decay $h \rightarrow b\bar{b}$ with and without the cuts defined in Eq. (31) in `MadGraph` at the parton level. Therefore, the acceptance is given by the ratio of the predicted $4b + Z$ events with and without cuts. The obtained values of the acceptances \mathcal{A} for the studied BPs are given in Tab. 3.

	P1	P2	P3	P4	P5	P6	P7	P8
\mathcal{A}	0.7308	0.7382	0.7376	0.7638	0.7725	0.7625	0.7963	0.7982

Table 3: Detector acceptances at the ILC1000 (see text) for the benchmark points defined in Tab. 2.

To evaluate the potential sensitivity to the H resonant peak, and therefore to λ_{hhH} , of the ILC1000 we again use the “theoretical estimator” R defined in Eq. (28). Analogously to the HL-LHC case, \bar{N}_i^R and \bar{N}_i^C denote the expected events, as defined in Eq. (30), in the i th bin from the purely resonant diagrams (the one mediated by H and proportional to λ_{hhH}) and the non-resonant ones, respectively.⁸ In contrast to the HL-LHC, in the case of the ILC1000 we define the signal region such that the difference between the resonant and non-resonant number of expected events is at least two, i.e.,

$$|\bar{N}_i^R - \bar{N}_i^C| > 2. \quad (32)$$

Here it should be kept in mind that, similar to the HL-LHC case, the “theoretical estimator” R gives an idea of how prominent the H resonance peak is relative to the continuum contributions from the non-resonant diagrams. Large values of R indicate more accessible H resonance peaks at the ILC1000, which implies higher chances of obtaining potential experimental information about the λ_{hhH} coupling. As in the case of the HL-LHC, R does not correspond to a true “experimental significance”.

4.2 Analysis of m_{hh}

In this subsection we analyze the differential m_{hh} distributions for the eight benchmark points as defined in Tab. 2 at the ILC1000. In Fig. 15 and Fig. 16, we present the results for P1–P4 and P5–P8, respectively. In each plot the red curve corresponds to the full RxSM prediction (σ_{RxSM}), whereas the green and the blue curves show, respectively, the results leaving out the resonant H diagram (σ_{NoH}) and taking into account the resonant H diagram only (σ_{H}). For comparison, the green curve indicates the SM result (σ_{SM}). The values for the total cross sections are given in the legends, as well as the values of m_H , κ_λ and λ_{hhH} for each benchmark point. The binning of 6.7 GeV is chosen according to Eq. (32).

⁸Note that the definition of \bar{N}^C slightly differs from the one used in the HL-LHC analysis, where the SM curve was employed for N^C . However, this has a minor numerical impact.

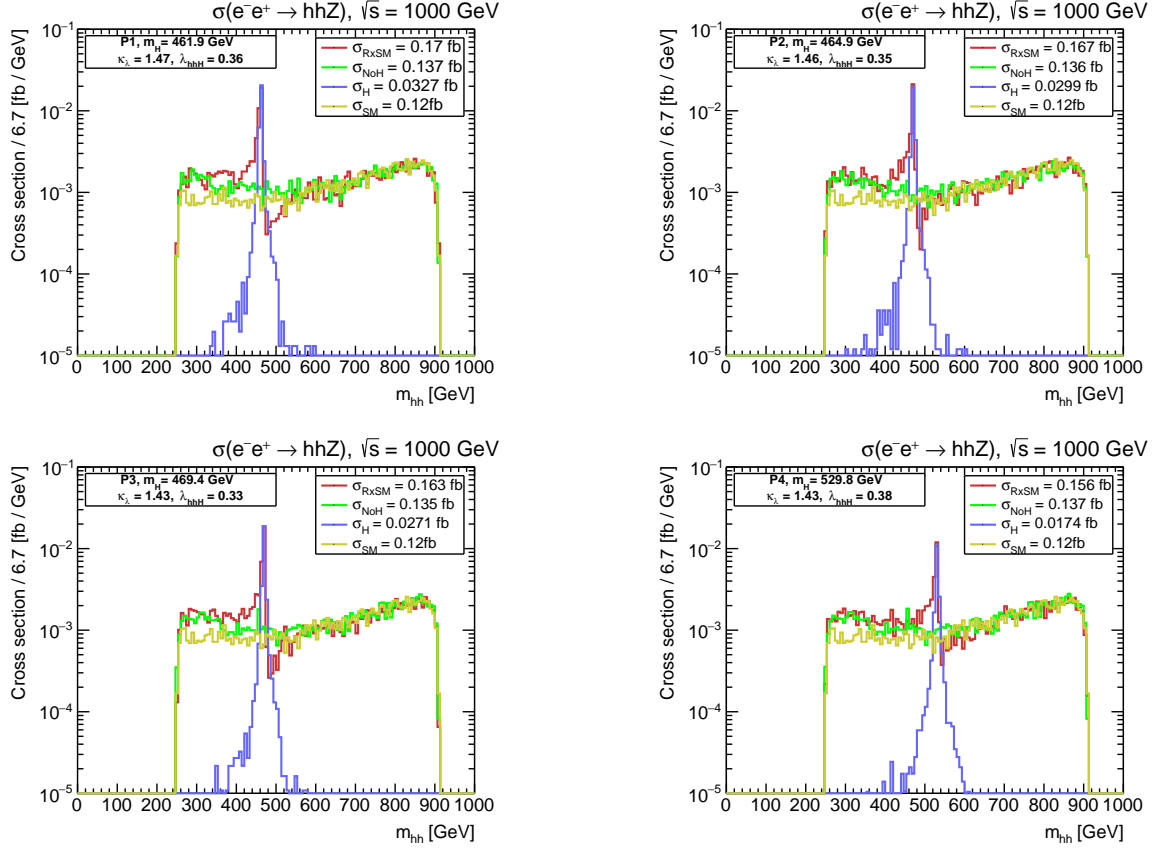


Figure 15: Differential cross section of the process $e^+e^- \rightarrow Zhh$ at the ILC1000 as a function of m_{hh} for the SM, for the pure heavy Higgs resonant contribution (blue), for the non-resonant contributions (green), and for the full RxSM calculation (red) for benchmark points P1, P2, P3, and P4.

Each benchmark point yields the same qualitative features, but differs in the location of the resonance structure, determined by the respective m_H value, the “height” of the resonance, determined by $\sin\theta \cdot \lambda_{hhH}$ and m_H , where the same holds for σ_H . For the two RxSM cross sections involving the h exchange (σ_{RxSM} , σ_{NoH}) κ_λ plays a significant role. The effects of $\kappa_\lambda \sim 1.45$ are best visible in the comparison of σ_{SM} and σ_{NoH} . As expected (and also observed in Ref. [35]), the enhancement w.r.t. the SM is most pronounced for small m_{hh} and leads to an enhancement of the differential cross section prediction (corresponding to an enhanced total cross section, as known for $\kappa_\lambda > 1$ in the $e^+e^- \rightarrow Zhh$ channel). This effect is nearly identical for all eight benchmark points, as the value of κ_λ varies only slightly over the whole benchmark plane.

The differential cross section that would be given by the pure resonance contribution is shown by the blue curves in Figs. 15 and (16). One can observe that this cross section is largest for smaller λ_{hhH} . As discussed above, this is due to the fact that in our benchmark plane larger λ_{hhH} corresponds to larger m_H , while $(\sin\theta \cdot \lambda_{hhH})$ remains approximately constant, leading to an overall suppression of the heavy Higgs-boson resonant contribution for larger λ_{hhH} . Taking into account the interference with the non-resonant diagrams, this yields a peak-dip

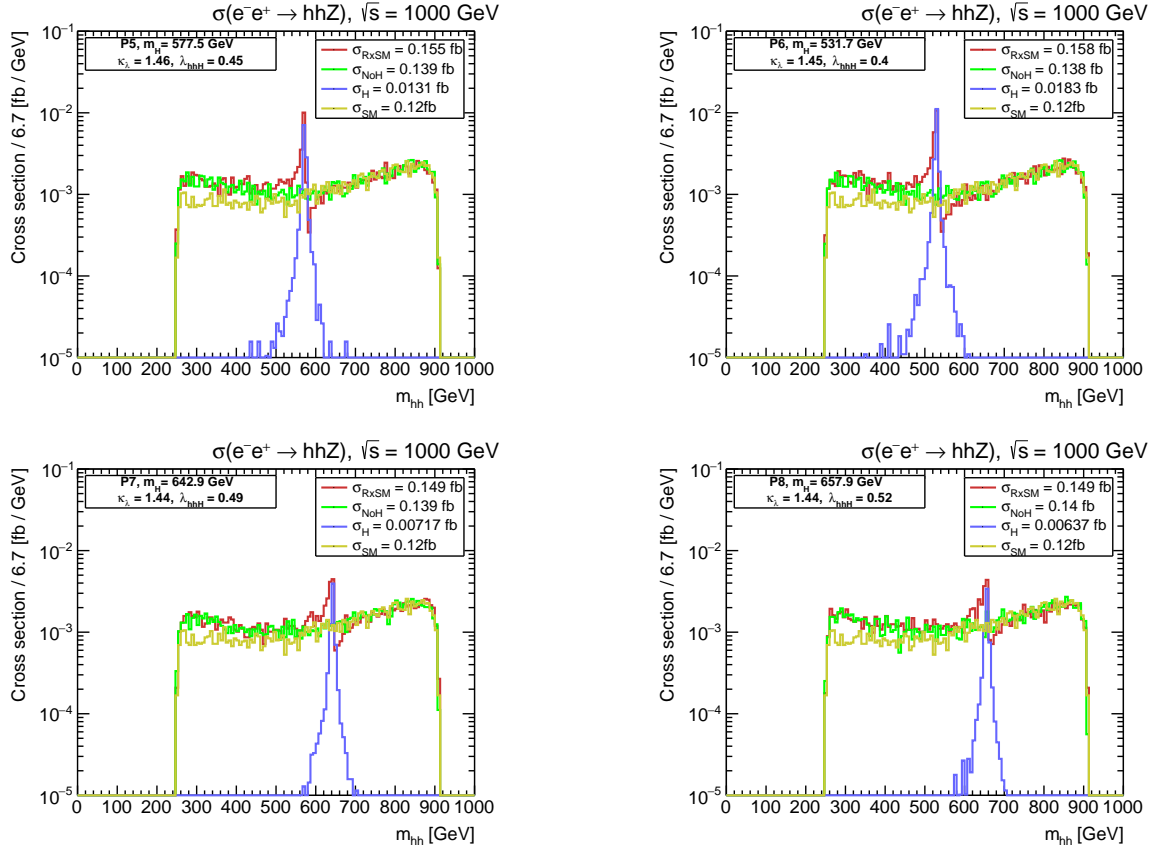


Figure 16: m_{hh} distribution for benchmark points P5 - P8, with the color coding as in Fig. 15.

structure around $m_{hh} = m_H$ as clearly visible in the red curves. However, corresponding to the size of the H -resonance contribution, also the peak-dip structure is strongest for smaller λ_{hhH} , which can be seen best in the R values: for each of the points we have evaluated the R value according to Eq. (28), which are summarized in Tab. 4. For an easier comparison, we also repeat in that table the values of m_H and λ_{hhH} for each benchmark point. It can be observed that within our benchmark plane (which is favored by the phenomenology of a strong FOEWPT) smaller values of λ_{hhH} lead (to a good approximation) to a stronger “signal” of the resonant H contribution and thus to a larger R value – in agreement with our discussion above. The overall substantially lower values of R as compared to the HL-LHC result on the one hand from a more realistic set-up including cuts etc., and on the other hand from the overall lower number of events at the e^+e^- collider.

	P1	P2	P3	P4	P5	P6	P7	P8
R	13.59	14.35	10.54	7.16	5.75	7.26	3.39	3.70
m_H [GeV]	461.9	470.8	469.4	530.9	575.1	529.6	642.5	656.1
λ_{hhH}	0.36	0.35	0.33	0.38	0.45	0.40	0.49	0.52

Table 4: Values of the sensitivity R for the eight benchmark points, see Tab. 2.

5 Conclusions

In this work we have analyzed the impact of triple Higgs couplings on the production cross section of two ~ 125 GeV Higgs bosons at the HL-LHC and the ILC1000. We have chosen the Higgs singlet extension of the SM without Z_2 symmetry, the RxSM, as an example framework. We have focused on a benchmark plane that is phenomenologically favored, as it yields a strong FOEWPT in the early universe (based on the original analysis of Ref. [25]), a key ingredient to fulfill one of the three Sakharov conditions required for EW baryogenesis to explain the baryon asymmetry of the universe. We have ensured that the plane under consideration is in agreement with all theoretical and experimental constraints. By the requirement of the FOEWPT the benchmark plane is not in the alignment limit. The main idea of our work is to analyze the effect of the THC, encoded in $\kappa_\lambda \equiv \lambda_{hhh}/\lambda_{\text{SM}}$, which is found to be $\kappa_\lambda \sim 1.45$, i.e. far away from the SM value. The second focus is on the impact of the BSM THC λ_{hhH} , which enters via a heavy Higgs-boson exchange with the subsequent decay $H \rightarrow hh$, in the di-Higgs production cross section both at the HL-LHC and at the ILC.

For the HL-LHC we calculated $\sigma(gg \rightarrow hh)$ as well as $d\sigma(gg \rightarrow hh)/dm_{hh}$ with the help of the code HPAIR, adapted to the RxSM. Within our phenomenologically favored benchmark plane the total cross section can deviate by more than 3σ from the SM cross section. In other parts of the benchmark plane the total cross section would remain experimentally indistinguishable from the SM prediction. Since we are away from the alignment limit, this equality between the RxSM and the SM results is due to (accidental) cancellations of the two BSM effects stemming from $\kappa_\lambda > 1$ and from the contribution of the heavy Higgs-boson resonance, inducing a dependence on λ_{hhH} .

This effect becomes better visible in the second part of the HL-LHC analysis, focusing on the m_{hh} distributions. These have been evaluated for eight benchmark points, distributed over our benchmark plane. For those we take into account a 15% detector smearing and a 50 GeV binning in m_{hh} . The eight benchmark points are compared with the SM expectation. A simple “theoretical significance”, R , is employed (as defined and used in an 2HDM HL-LHC analysis in Ref. [20]) that allows us to estimate the “visibility” of the H -resonance peak w.r.t. the SM expectation. While this does not constitute a realistic experimental significance, this estimator allows to compare different benchmark points with each other (as well as collider energy and luminosity options). The large values found for R in our eight benchmark points, spanning the whole plane favored by the FOEWPT, give rise to the hope that also in a realistic experimental analysis a clear sign of the H -resonance peak can be observed, giving access to the BSM THC λ_{hhH} .

In the final step of our HL-LHC analysis in the RxSM we compare the m_{hh} distributions evaluated solely from the resonance diagram, but neglecting the two continuum diagrams with the results from the full calculation (i.e. taking into account all contributing diagrams and in particular the corresponding interferences). This approach of neglecting the continuum diagrams is currently taken by the experimental collaborations, ATLAS and CMS, to obtain their results for resonant di-Higgs production. In the context of the 2HDM, in Ref. [21] it was demonstrated that this approach can lead to the erroneous exclusion of parameter points. In our RxSM analysis, comparing the m_{hh} distributions either neglecting or including the continuum diagrams, we find (as expected) strong and relevant differences between the two types of distributions. In particular, in the full calculation the “resonance peak” is

substantially broadened. This sheds severe doubts that the current experimental data from resonant di-Higgs production at the LHC can readily be applied to our phenomenologically favored benchmark plane in the RxSM.

The analysis of the RxSM benchmark plane featuring a strong FOEWPT was subsequently extended to future e^+e^- colliders. As a particular example we focused on the ILC with a center-of-mass energy of $\sqrt{s} = 1000$ GeV, the ILC1000. As an integrated luminosity we assume 8 ab^{-1} . The center-of-mass energy is required since our benchmark points have m_H values that yield a resonant contribution (and thus possibly access to λ_{hhH}) only for $\sqrt{s} \gtrsim 600$ GeV (depending on m_H), making the ILC1000 the preferred option. From the total ILC1000 cross section alone, in our benchmark plane we find a deviation w.r.t. the SM prediction between ~ 2 and 4σ . Also for the ILC1000 we calculated the m_{hh} distributions for the eight benchmark points, evaluating the “theory estimator” R adapted to the e^+e^- case (following a corresponding 2HDM analysis in Ref. [36]). In this case also experimental cuts were included to take into account detector efficiencies etc. (again following Ref. [36]). We find that for the eight benchmark points, to a good approximation, smaller values of λ_{hhH} lead to a stronger “signal” of the resonant H -exchange contribution and thus to a larger R value. Overall substantially lower values of R as compared to the HL-LHC result are found. This results on the one hand from a more realistic set-up including cuts etc., and on the other hand from the overall lower number of events at the e^+e^- collider. Nevertheless, as in the HL-LHC case this gives rise to the hope that also in a realistic experimental analysis a clear sign of the H -resonance peak can be observed, giving access to the BSM THC λ_{hhH} at the ILC1000.

Overall, we conclude that within the RxSM, depending on the values of the underlying Lagrangian parameters, a sizable resonant H contribution to the di-Higgs production cross section of two SM-like Higgs bosons can leave possibly visible effects in the m_{hh} distribution. This applies to the HL-LHC or to a future e^+e^- collider (taking the ILC1000 as a concrete example). This would pave the way for a first determination of a BSM THC, a step that is crucial for the reconstruction of the Higgs potential of the underlying BSM model.

Acknowledgements

We thank M. Ramsey Musolf for helpful discussions. F.A. acknowledge support by the Deutsche Forschungsgemeinschaft (DFG, German Research Foundation) under Germany’s Excellence Strategy — EXC 2121 “Quantum Universe” — 390833306. This work has been partially funded by the Deutsche Forschungsgemeinschaft (DFG, German Research Foundation) - 491245950. S.H. acknowledges partial financial support by the Spanish Research Agency (Agencia Estatal de Investigación) through the grant IFT Centro de Excelencia Severo Ochoa No CEX2020-001007-S funded by MCIN/AEI/10.13039/501100011033. The work of S.H. was also supported by the Grant PID2022-142545NB-C21 funded by MCIN/AEI/10.13039/501100011033/ FEDER, UE. The work of M.M. has been supported by the BMBF-Project 05H24VKB. The work of A.V.S. is supported is in part by the Deutsche Forschungsgemeinschaft (DFG, German Research Foundation) Emmy Noether Grant No. BR 6995/1-1, and under Germany’s Excellence Strategy — EXC 2121 “Quantum Universe” — 390833306, and in part by the Deutsche Forschungsgemeinschaft (DFG, German Research Foundation) — 491245950.

References

- [1] G. Aad *et al.* [ATLAS Collaboration], Phys. Lett. B **716** (2012) 1 [arXiv:1207.7214 [hep-ex]].
- [2] S. Chatrchyan *et al.* [CMS Collaboration], Phys. Lett. B **716** (2012) 30 [arXiv:1207.7235 [hep-ex]].
- [3] G. Aad *et al.* [ATLAS and CMS Collaborations], JHEP **1608** (2016) 045 [arXiv:1606.02266 [hep-ex]].
- [4] K. Kajantie, M. Laine, K. Rummukainen and M. E. Shaposhnikov, Phys. Rev. Lett. **77** (1996), 2887-2890 [arXiv:hep-ph/9605288 [hep-ph]].
- [5] V. A. Kuzmin, V. A. Rubakov and M. E. Shaposhnikov, Phys. Lett. B **155** (1985), 36.
- [6] J.R. Espinosa, M. Quiros, Lett. B **305** (1993) 98, [hep-ph/9301285].
- [7] S. Profumo, M.J. Ramsey-Musolf, G. Shaughnessy, JHEP **08** (2007) 010, [arXiv:0705.2425 [hep-ph]].
- [8] J.R. Espinosa, M. Quiros, Phys. Rev. D **76** (2007) 076004, [hep-ph/0701145].
- [9] S.R. Espinosa, T. Konstandin, F. Riva Nucl. Phys. B **854** (2012) 592, [arXiv:1107.5441 [hep-ph]].
- [10] D. Curtin, P. Meade, C.-T. Yu, JHEP **11** (2014) 127, [arXiv:1409.0005 [hep-ph]].
- [11] G. Kurup, M. Perelstein, Phys. Rev. D **96** (2017) 015036, [arXiv:1704.03381 [hep-ph]].
- [12] S.W. Ham, Y.S. Jeong, S.K. Oh, J. Phys. G **31** (2005) 857, [hep-ph/0411352].
- [13] V. Barger, P. Langacker, M. McCaskey, M.J. Ramsey-Musolf, G. Shaughnessy, Phys. Rev. D **79** (2009) 015018, [arXiv:0811.0393 [hep-ph]].
- [14] A.D. Shakharov, Pisma Zh. Eksp. Teor. Fiz. **5** (1967) 32.
- [15] ATLAS Collaboration, Phys.Rev.Lett. **133** (2024) 10, 101801 [arXiv:2406.09971 [hep-ex]].
- [16] CMS Collaboration, (2024), [CMS-PAS-HIG-20-011].
- [17] H. Abouabid *et al.*, JHEP **09** (2022), 011 [arXiv:2112.12515 [hep-ph]].
- [18] J. de Blas *et al.*, JHEP **01** (2020), 139 [arXiv:1905.03764 [hep-ph]].
- [19] B. Di Micco, *et al.* Rev. Phys. **5** (2020), 100045 [arXiv:1910.00012 [hep-ph]].
- [20] F. Arco, S. Heinemeyer, M. Mühlleitner and K. Radchenko, Eur. Phys. J. C **83** (2023) no.11, 1019 [arXiv:2212.11242 [hep-ph]].
- [21] S. Heinemeyer, M. Mühlleitner, K. Radchenko and G. Weiglein, [arXiv:2403.14776 [hep-ph]].

- [22] A. M. Sirunyan *et al.* [CMS], JHEP **06** (2018), 127 [erratum: JHEP **03** (2019), 128], [arXiv:1804.01939 [hep-ex]].
- [23] R. N. Lerner, J. McDonald, Phys.Rev.D **80** (2009), 123507, [arXiv:0909.0520].
- [24] R. Costa, M. Mühlleitner, M. O. P. Sampaio and R. Santos, JHEP **06** (2016), 034 [arXiv:1512.05355 [hep-ph]].
- [25] H. L. Lin, M. J. Ramsey-Musolf, S. Willocq, Phys.Rev.D **100** (2019) 7, 075035 [arXiv:1906.05289 [hep-ph]].
- [26] A. Alves, T. Ghosh, H.K. Guo, K. Sinha, D. Vagie, JHEP **04** (2019) 052, [arXiv:1812.09333 [hep-ph]].
- [27] T. Plehn, M. Spira, P.M. Zerwas Nucl.Phys.B **479** (1996), 46-64, [erratum: Nucl.Phys.B **531** (1998), 655-655], [arXiv:9603205 [hep-ph]].
- [28] S. Dawson, S. Dittmaier, M. Spira, Phys.Rev.D **58** (1998), 115012, [arXiv: [hep-ph]].
- [29] P. Bambade *et al.* [arXiv:1903.01629 [hep-ex]].
- [30] P. N. Burrows *et al.* [CLICdp and CLIC] [arXiv:1812.06018 [physics.acc-ph]].
- [31] A. Djouadi, W. Kilian, M. Mühlleitner, and P. M. Zerwas, Eur. Phys. J. C **10**, 27-43 (1999) [arXiv:hep-ph/9903229 [hep-ph]].
- [32] H. Abramowicz *et al.*, Eur. Phys. J. C **77** (2017) no.7, 475 [arXiv:1608.07538 [hep-ex]].
- [33] J. Strube [ILC Physics and Detector Study], Nucl. Part. Phys. Proc. **273-275** (2016), 2463-2465
- [34] P. Roloff *et al.* [CLICdp], Eur. Phys. J. C **80** (2020) no.11, 1010 [arXiv:1901.05897 [hep-ex]].
- [35] F. Arco, S. Heinemeyer and M. J. Herrero, Eur. Phys. J. C **81** (2021) no.10, 913 [arXiv:2106.11105 [hep-ph]].
- [36] F. Arco, S. Heinemeyer, M. J. Herrero, Eur. Phys. J. C **82** (2022) 6, 536, [arXiv:2203.12684 [hep-ph]].
- [37] A. Djouadi, W. Kilian, M. Mühlleitner, and P.M. Zerwas, Eur. Phys. J. C. **10** (1999), 45 [hep-ph/9904287 [hep-ph]].
- [38] P. Basler, M. Mühlleitner, J. Wittbrodt, JHEP **03** (2018), 061 [arXiv:1711.04097 [hep-ph]].
- [39] P. Basler, M. Mühlleitner, J. Müller, JHEP **05** (2020), 016 [arXiv:1912.10477 [hep-ph]].
- [40] W. Zhang, H. L. Li, K. Liu, M. J. Ramsey-Musolf, Y. Zeng and S. Arunasalam, JHEP **12** (2023), 018 [arXiv:2303.03612 [hep-ph]].

- [41] P. Palit and S. Shil, *J. Phys. G* **51** (2024) no.9, 095005 [arXiv:2302.04191 [hep-ph]].
- [42] J. Ellis, M. Lewicki, M. Merchand, J. M. No and M. Zych, *JHEP* **01** (2023), 093
- [43] L. Niemi and T. V. I. Tenkanen, [arXiv:2408.15912 [hep-ph]].
- [44] O. Gould and P. Saffin, [arXiv:2411.08951 [hep-ph]].
- [45] A. Giovanakis, *Phys. Dark Univ.* **46** (2024), 101682 [arXiv:2410.04428 [hep-ph]].
- [46] L. Niemi, M. J. Ramsey-Musolf and G. Xia, *Phys. Rev. D* **110** (2024) no.11, 115016 [arXiv:2405.01191 [hep-ph]].
- [47] M. J. Ramsey-Musolf, T. V. I. Tenkanen and V. Q. Tran, [arXiv:2409.17554 [hep-ph]].
- [48] F. Feuerstake, E. Fuchs, T. Robens and D. Winterbottom, [arXiv:2409.06651 [hep-ph]].
- [49] I. M. Lewis, J. Scott, M. A. S. Alcaraz and M. Sullivan, [arXiv:2410.08275 [hep-ph]].
- [50] M. Aboudonia, C. Balazs, A. Papaefstathiou and G. White, [arXiv:2410.22700 [hep-ph]].
- [51] M. Gonderinger, Y. Li, H. Patel, M. J. Ramsey-Musolf, *JHEP* **01** (2010), 053, [arXiv:0910.3167 [hep-ph]].
- [52] P. Bechtle, O. Brein, S. Heinemeyer, G. Weiglein and K. E. Williams, *Comput. Phys. Commun.* **181** (2010) 138 [arXiv:0811.4169 [hep-ph]].
- [53] P. Bechtle, O. Brein, S. Heinemeyer, G. Weiglein and K. E. Williams, *Comput. Phys. Commun.* **182** (2011) 2605 [arXiv:1102.1898 [hep-ph]].
- [54] P. Bechtle, O. Brein, S. Heinemeyer, O. Stål, T. Stefaniak, G. Weiglein and K. E. Williams, *Eur. Phys. J. C* **74** (2014) no.3, 2693 [arXiv:1311.0055 [hep-ph]].
- [55] P. Bechtle, S. Heinemeyer, O. Stål, T. Stefaniak and G. Weiglein, *Eur. Phys. J. C* **75** (2015) no.9, 421 [arXiv:1507.06706 [hep-ph]].
- [56] P. Bechtle, D. Dercks, S. Heinemeyer, T. Klingl, T. Stefaniak, G. Weiglein and J. Wittbrodt, *Eur. Phys. J. C* **80** (2020) no.12, 1211 [arXiv:2006.06007 [hep-ph]].
- [57] H. Bahl, T. Biekötter, S. Heinemeyer, C. Li, S. Paasch, G. Weiglein and J. Wittbrodt, *Comput. Phys. Commun.* **291** (2023), 108803 [arXiv:2210.09332 [hep-ph]].
- [58] P. Bechtle, S. Heinemeyer, O. Stål, T. Stefaniak and G. Weiglein, *Eur. Phys. J. C* **74** (2014) no.2, 2711 [arXiv:1305.1933 [hep-ph]].
- [59] P. Bechtle, S. Heinemeyer, O. Stål, T. Stefaniak and G. Weiglein, *JHEP* **1411** (2014) 039 [arXiv:1403.1582 [hep-ph]].
- [60] P. Bechtle, S. Heinemeyer, T. Klingl, T. Stefaniak, G. Weiglein and J. Wittbrodt, *Eur. Phys. J. C* **81** (2021) no.2, 145 [arXiv:2012.09197 [hep-ph]].

- [61] P. Basler and M. Mühlleitner, *Comput. Phys. Commun.* **237** (2019), 62-85 [arXiv:1803.02846 [hep-ph]].
- [62] P. Basler, M. Mühlleitner and J. Müller, *Comput. Phys. Commun.* **269** (2021), 108124 [arXiv:2007.01725 [hep-ph]].
- [63] P. Basler, L. Biermann, M. Mühlleitner, J. Müller, R. Santos and J. Viana, [arXiv:2404.19037 [hep-ph]].
- [64] ATLAS Collaboration, *Eur.Phys.J.C* **81** (2021) 4, 332, [arXiv:2009.14791 [hep-ex]].
- [65] D. T. Nhung, M. Mühlleitner, J. Streicher and K. Walz, *JHEP* **11** (2013), 181 [arXiv:1306.3926 [hep-ph]].
- [66] R. Gröber, M. Mühlleitner, M. Spira and J. Streicher, *JHEP* **09** (2015), 092 [arXiv:1504.06577 [hep-ph]].
- [67] R. Gröber, M. Mühlleitner, M. Spira, *Nucl.Phys.B* **925** (2017), 1-27, [arXiv:1705.05314 [hep-ph]].
- [68] S. Borowka, N. Greiner, G. Heinrich, S. P. Jones, M. Kerner, J. Schlenk, U. Schubert and T. Zirke, *Phys. Rev. Lett.* **117** (2016) no.1, 012001 [erratum: *Phys. Rev. Lett.* **117** (2016) no.7, 079901] [arXiv:1604.06447 [hep-ph]].
- [69] S. Borowka, N. Greiner, G. Heinrich, S. P. Jones, M. Kerner, J. Schlenk and T. Zirke, *JHEP* **10** (2016), 107 [arXiv:1608.04798 [hep-ph]].
- [70] J. Baglio, F. Campanario, S. Glaus, M. Mühlleitner, M. Spira and J. Streicher, *Eur. Phys. J. C* **79** (2019) no.6, 459 [arXiv:1811.05692 [hep-ph]].
- [71] J. Baglio, F. Campanario, S. Glaus, M. Mühlleitner, J. Ronca, M. Spira and J. Streicher, *JHEP* **04** (2020), 181 [arXiv:2003.03227 [hep-ph]].
- [72] J. Baglio, F. Campanario, S. Glaus, M. Mühlleitner, J. Ronca and M. Spira, *Phys. Rev. D* **103** (2021) no.5, 056002 [arXiv:2008.11626 [hep-ph]].
- [73] J. Baglio, F. Campanario, S. Glaus, M. Mühlleitner, J. Ronca, M. Spira, *Eur. Phys. J. C* **83** (2023) 9, 826, [arXiv:2303.05409 [hep-ph]].
- [74] J. Baglio, F. Campanario, S. Glaus, M. Mühlleitner, J. Ronca and M. Spira, *PoS PANIC2021* (2022), 393.
- [75] G. Buchalla, M. Capozzi, A. Celis, G. Heinrich and L. Scyboz, *JHEP* **09** (2018), 057 [arXiv:1806.05162 [hep-ph]].
- [76] M. Cepeda *et al.* *CERN Yellow Rep. Monogr.* **7**, 221-584 (2019) [arXiv:1902.00134 [hep-ph]].
- [77] [ATLAS], ATLAS-CONF-2022-050.
- [78] [CMS], *Nature* **607** (2022), 7917, p. 60 [arXiv:2207.00043 [hep-ex]].

- [79] J. Alwall, R. Frederix, S. Frixione, V. Hirschi, F. Maltoni, O. Mattelaer, H. S. Shao, T. Stelzer, P. Torrielli and M. Zaro, JHEP **07** (2014), 079 [arXiv:1405.0301 [hep-ph]].
- [80] F. Staub, Comput. Phys. Commun. **185** (2014), 1773-1790 [arXiv:1309.7223 [hep-ph]].
- [81] H. Baer *et al.* [ILC], [arXiv:1306.6352 [hep-ph]].
- [82] G. Moortgat-Pick, H. Baer, M. Battaglia, G. Belanger, K. Fujii, J. Kalinowski, S. Heinemeyer, Y. Kiyo, K. Olive and F. Simon, *et al.* Eur. Phys. J. C **75** (2015) no.8, 371 [arXiv:1504.01726 [hep-ph]].
- [83] C. F. Dürig, doi:10.3204/PUBDB-2016-04283